

Davis Trenton (Orcid ID: 0000-0001-7489-5079)

Rutledge Steven A. (Orcid ID: 0000-0001-7397-2802)

Fuchs Brody Robert (Orcid ID: 0000-0002-7629-0687)

**Lightning location, NO_x production, and transport by anomalous and normal polarity
thunderstorms**

Trenton C. Davis¹, Steven A. Rutledge and Brody R. Fuchs

Submitted to Journal of Geophysical Research: Atmospheres (Revision)

Department of Atmospheric Science, Colorado State University, Fort Collins, Colorado

¹U.S. National Weather Service Weather Forecasting Office, Mount Holly, New Jersey

Main points

Flash channels are derived from LMA observations to generate lightning-produced NO_x in air parcels of normal and anomalous polarity storms

Higher flash rates and stronger updrafts lead to a striking increase in LNO_x transport to the upper troposphere in anomalous storms

LNO_x produced by compact flashes are slightly lower than previous estimates of LNO_x produced per flash

¹Corresponding author email: Trenton.davis@noaa.gov

This article has been accepted for publication and undergone full peer review but has not been through the copyediting, typesetting, pagination and proofreading process which may lead to differences between this version and the Version of Record. Please cite this article as doi: 10.1029/2018JD029979

Abstract

Production and transport of NO_x by convection is critical as it serves as a precursor to tropospheric ozone, an important greenhouse gas. Lightning serves as the largest source of nitrogen oxides ($\text{NO}_x = \text{NO} + \text{NO}_2$) to the upper troposphere (UT) and is one of the largest natural sources of NO_x . Interest is placed on the vertical advection of NO_x because its lifetime increases to several days in the UT compared to roughly three hours in the lower troposphere and boundary layer. Thus, lightning can play an important role in ozone production within the UT. However, the amount of NO_x produced per flash and NO_x advection in storms remain uncertain. This study investigates lightning NO_x (LNO_x) production and transport processes in anomalous (mid-level positive charge) and normal polarity (mid-level negative charge) thunderstorms by advecting parcels containing LNO_x from the flash channels of over 5600 lightning flashes observed during the Deep Convective Clouds and Chemistry (DC3) field campaign. Results reveal most flash channels occur near 6-8 km in the normal polarity thunderstorms and 5-6 km within anomalous polarity thunderstorms. Larger flash rates and stronger updrafts in anomalous storms result in considerably larger LNO_x mixing ratios (peaks of 0.75-1.75 ppb) in the UT compared to normal polarity storms (peaks < 0.5 ppb). A slightly lower mean flash LNO_x production was also found among all five storms in this study (storm mean values of 72-158 moles per flash) compared to previous estimates, which generally parameterize LNO_x by flash rate rather than flash rate.

1. Introduction

As numerical modeling continues to improve, atmospheric chemists and climate scientists are beginning to better understand the sources and sinks of the many critical atmospheric gases such as ozone. In this section, we will explore how nitrogen oxides ($\text{NO}_x = \text{NO} + \text{NO}_2$), one of the important sources of tropospheric ozone, is currently parameterized. From there, we will explore some of the challenges faced by these current methodologies, including the differences in charge structure within normal and anomalous polarity thunderstorms.

1.1 LNO_x Background

NO_x remains heavily researched because they serve as a catalytic precursor to ozone (O_3), which acts as a greenhouse gas in the upper troposphere (Labrador et al., 2005; Schumann and Huntrieser, 2007; Buffen et al., 2014). Globally, lightning is the greatest natural source of NO_x in the upper troposphere (UT), yet the amount and transport of LNO_x produced by individual flashes remain highly uncertain (Lawrence et al., 1995; Price et al., 1997; DeCaria et al., 2005; Schumann and Huntrieser, 2007; Buffen et al., 2014). Research suggests the lifetime of NO_x approaches several days close to the tropopause, allowing for greater ozone production (Ridley et al., 1996; Schumann and Huntrieser, 2007). However, if LNO_x is transported by downdrafts or is formed near the surface, its lifetime is roughly three hours, rendering it of reduced importance to ozone production (DeCaria et al., 2000; Schumann and Huntrieser, 2007; Nault et al., 2017). Wu et al. (2007) showed in a global ozone study that LNO_x is roughly six times more efficient than anthropogenic NO_x emissions in producing upper tropospheric ozone due to its production in the UT. Thus, to understand the impact of deep convection on ozone production, one must not only consider LNO_x production, but subsequent transport by storm scale updrafts and downdrafts (Pickering et al., 1998; Barthe and Barth, 2008).

The impact of LNO_x on tropospheric ozone is primarily studied through numerical model simulations, aimed at improving the timing and placement of LNO_x within simulated thunderstorms via parameterizations (Ott et al., 2010; Barthe and Barth, 2008; Pickering et al., 1998). Numerous parameterizations for LNO_x production have been developed, but the following describes perhaps the

most common methodology. Parameterizing lightning flash rate is usually the first step in this process and is generally a function of one of more storm parameters such as reflectivity volume (Basarab et al., 2015), storm cloud top height (Price and Rind, 1992), convective ice mass flux (Deierling et al., 2008), updraft speed (e.g. Price and Rind, 1992; Pickering et al., 1998), or instability (e.g. Fuchs et al., 2015). The total flash rate is partitioned into intra-cloud (IC) and cloud-to-ground (CG) flashes using a predetermined ratio found from previous studies, often varying geographically (e.g. Pickering et al., 1998; DeCaria et al., 2000, 2005; Bocippio et al., 2001). Next, the vertical distribution of flash channels is prescribed for both flash types, thus partitioning the channel components of each type of flash into the storm's vertical dimension (e.g. Price et al., 1997; Pickering et al., 1998). These profiles define the fraction of the total flash channel length (FCL) for each flash (IC, CG, or both depending on whether flash type is known) that exists at each vertical model level. However, some studies bypass this route, distributing a prescribed LNO_x mass in the vertical for each type of flash (e.g. Ott et al., 2010). Once FCL is developed as a function of height, LNO_x is prescribed as a function of FCL. NO_x is then advected by the simulated cloud air motions.

FCL within thunderstorms is highly variable, many times more so than flash rate itself, often depending on environmental characteristics governing the charge separation process. Recent work by Carey et al. (2016) suggests that total flash rate may be well correlated to storm intensity while flash extent might not be at times. Several studies have investigated changes in FCL profiles, but sensitivity of final LNO_x concentration to initial placement remains unclear (e.g. Pickering et al., 1998; Fehr et al., 2004; Labrador et al., 2005; Ott et al., 2007; Hansen et al., 2010; Ott et al., 2010; Mecikalski et al., 2017; Fuchs and Rutledge, 2018). For example, Hansen et al. (2010) found the vertical structure of flashes to vary, with more intense thunderstorms having a bi-modal flash extent distribution compared to the predominant unimodal distribution seen in less intense thunderstorms-suggesting a correlation in vertical charge structure to storm intensity.

In the horizontal dimension, many studies tend to restrict flash channels and/or LNO_x production within reflectivity echoes > 20 dBZ (20 dBZ echo volume), following the findings of MacGorman and Rust (1998) (e.g. DeCaria et al., 2000, 2005). Thus, LNO_x parameterizations involving FCL often produce LNO_x according to a defined vertical profile based upon the altitude (pressure), and

temperature of each level, all while assuming a fixed flash current and that all flash channels occur within the 20 dBZ echo volume (Wang et al., 1998; DeCaria et al., 2000). Mecikalski and Carey (2018a, b) found that in general, flashes tend to propagate from higher to lower reflectivity, regardless of flash type, further suggesting that increased focus on flash extent is needed rather than singly flash initiation. Additional research on the relatively newer hybrid flash categorization shows a greater likelihood for flash extent outside of the 20 dBZ echo volume (Mecikalski and Carey, 2017). Other efforts to improve LNO_x parameterizations have been implemented, such as attempting to account for the tortuous nature of flash channels (Ott et al., 2007) and the filamentary structure of lightning channels (Barthe and Barth, 2008; Ott et al., 2010; Bruning and Thomas, 2015).

Considerable uncertainty remains in our understanding of the advection processes governing LNO_x redistribution after formation from FCL. This poses significant problems since downstream ozone production depends upon the height at which LNO_x resides. Furthermore, several studies have found highly variable vertical profiles of LNO_x after modeling with various parameterization schemes (Pickering et al., 1998; Barthe and Barth, 2008). Furthermore, Ott et al. (2010) found that the final advected LNO_x distribution varies with storm environment. In fact, several studies discuss the need for continued research focused on quantifying the impact of various environmentally-driven storm structures on the production of LNO_x (e.g. Ott et al., 2007; Barthe and Barth, 2008; Mecikalski et al., 2018b). Unfortunately, little research has been conducted to investigate the impact of environmental characteristics on LNO_x production, explaining why it became one of the main goals of the Deep Convective Clouds and Chemistry (DC3) campaign in 2012 (Barth et al., 2015).

Further uncertainty centers on LNO_x production per flash. In their summary article, Schumann and Huntrieser (2007) note that current estimates range from 33-660 moles, with a mean value of 250 moles. Values reported from other studies include 360 moles (Ott et al., 2007), and 60-570 moles (Pollack et al., 2016). Several studies suggest that IC and CG flashes may produce similar amounts of LNO_x (DeCaria et al., 2000, 2005; Ridley et al., 2005; Schumann and Huntrieser, 2007; Ott et al., 2007; Ott et al., 2010). However, other studies suggest that IC and CG flashes likely produce different amounts of LNO_x (Koshak et al., 2014; Carey et al., 2016; Mecikalski et al., 2017).

1.2 Anomalous versus normal polarity thunderstorms

The mechanisms for the reversal of charge structures from the normal dipole/tripole into an anomalous dipole/tripole has been a topic of considerable interest over the past decade and a half (e.g. Rust et al., 2005; Wiens et al., 2005; Tessendorf et al., 2007; MacGorman et al., 2008; Fuchs et al., 2015, Fuchs et al., 2018; Fuchs and Rutledge, 2018). While many areas of charge form within thunderstorms, it is accepted that these charge pockets align themselves within two or three heterogeneous charge layers in each storm structure. The spatial distribution and magnitude of these charge layers ultimately affect flash channel distribution and where subsequent LNO_x production occurs. In normal polarity thunderstorms, flashes tend to initiate between two of these charge layers: an upper-level region of positive charge and a mid-level negative charge region, although more complex structures with additional charge layers have been observed (Williams, 1989; Lang and Rutledge, 2011; Bruning et al., 2014). Research suggests this charge structure develops when graupel particles collide with smaller ice crystals in the presence of supercooled cloud droplets comprising the non-inductive charging mechanism (Takahashi, 1978; Jayaratne et al., 1983; Saunders et al., 1991; Takahashi, 2017). Negatively charged graupel particles produce the mid-level negative charge layer while the ascending ice crystals carry net positive charge to upper levels. Most thunderstorms possess this charge structure, leading to this “normal” label (Williams, 1989). In anomalous thunderstorms, higher supercooled liquid water (SCLW) contents (aided by shallow warm cloud depths that reduce warm rain production) is considered to promote positive charge on graupel (Saunders et al., 1991; Saunders and Peck, 1998). Ice crystals then carry negative charge to the upper levels, leading to a so-called inverted dipole.

Surface elevation may also play a role in determining the polarity structure of a thunderstorms, as areas of higher elevation, such as the High Plains and Front Range region of Colorado and Wyoming, tend to experience somewhat drier boundary layers (BLs) than the U.S. Southeast. The higher surface elevation of these areas also leads to shallow or non-existent warm cloud depths over this region, leading to higher cloud water contents in the mixed-phase region (Fuchs et al., 2018).

Ultimately, thunderstorm polarity controls the vertical distribution of flashes. In normal polarity thunderstorms, flash initiation is typically between 8-10 km versus 5-6 km in anomalous polarity thunderstorms (Mecikalski and Carey, 2017, 2018a; Mecikalski et al., 2018; Fuchs et al., 2018; Fuchs and Rutledge, 2018). Since the lifetime of NO_x increases with height, storms that produce more LNO_x at upper altitudes may be expected to have a larger impact on tropospheric ozone production compared to thunderstorms that produce more LNO_x at lower altitudes, such as anomalous storms. While many studies using numerical transport models have allowed for the advection of LNO_x , relatively little research has been conducted in regard to addressing these differences between normal and anomalous storms. NO_x transport using a multi-Doppler framework to obtain storm motions has been understudied as well. Indeed, these were major goals of the 2012 DC3 field campaign (Barth et al., 2015).

1.3 Goals of this study

In this study, we will examine the spatial distribution of flashes and LNO_x in both normal and anomalous thunderstorms to further understand the effect of environmentally-driven charge structure and dynamics on LNO_x production and transport. Specifically, this goal can be broken up into three sub-questions: (1) where does the bulk of the flash channel production occur and where is LNO_x formed in thunderstorms of normal vs. anomalous polarity? (2) Are there differences in the advection and amounts of LNO_x between normal and anomalous thunderstorms, especially to the UT? (3) Are there differences in the mean LNO_x production per flash between these two charge structures? To answer these questions, flash channel locations are investigated and a parcel trajectory analysis is used to assess LNO_x transport to the UT, which we define as heights ≥ 8 km above MSL. While several previous studies (e.g. Koshak et al., 2014; Carey et al., 2016) have investigated LNO_x production from LMA observations to reconstruct flashes and produce LNO_x based on FCL, this study also allows for the transport of this LNO_x based on observed storm relative winds using dual-Doppler radar.

2. Data and Methodology

While many thunderstorms were observed during the DC3 project throughout the summer of 2013, this dataset must be filtered such that only those storms with the most complete set of observations are selected so that these goals can be accurately investigated. As one would expect, there are many processes involved in this study which will be described within this section.

2.1 Selection of cases

Five storms are selected from the DC3 field campaign, which was conducted in May - June 2012 primarily in Alabama, Oklahoma, W. Texas, and Colorado (Barth et al., 2015). To be selected for this study, storms needed to remain isolated in nature throughout their lifetimes, remain within respective dual-Doppler lobes for at least one hour while also within the optimal detection range of the LMA networks (~ 125 km) throughout the entire lifetime of the storm, and produce a sufficient number of total flashes ($n_{fl} \geq 100$; Fuchs et al., 2015). The n_{fl} threshold was somewhat arbitrarily chosen such that enough flash parcels were created to observe trends in advection characteristics. Based on these criteria, 5645 lightning flashes from the five cases were gridded, resulting in 206,565 km of total channel segments. The three selected anomalous thunderstorms occurred on 6 June, 27 June, and 28 June 2012 in Colorado while the two normal polarity thunderstorms occurred on 18 May and 11 June 2012 in Alabama. Note that the latter two storms in Alabama are included in studies investigating integrated kinematic, microphysical, and lightning properties (Bain, 2013; Bain et al., 2013). Refer to Table 1 for a listing of various intensity parameters and environmental conditions for each storm.

Selection criteria for this study included isolated thunderstorms so that lightning flashes and their NO_x production could be properly attributed to individual storms, limiting overlap between nearby convective cells. Since a large portion of convective storms do not remain isolated, the applicability of these results to a large subset of storms in these two regions of the U.S. becomes difficult. Flashes were constructed using very high frequency (VHF) LMAs in northeast Colorado (COLMA) and Northern Alabama (NALMA). VHF sources emitted by electrical breakdown were grouped using spatial and temporal thresholds following Fuchs et al. (2016). Radar observations were provided by

the Colorado State University (CSU) CHILL and CSU Pawnee (S-band) radars in northern Colorado and the National Weather Service WSR-88D KHTX (S-band) and University of Alabama in Huntsville (UAH) ARMOR (C-band) radars in the northern Alabama region. Refer to Barth et al. (2015) for more information regarding DC3.

2.2 Radar attributions

The storm cells are tracked using an automated case-study framework so that radar-derived quantities and lightning flashes could be properly attributed to individual storms. The CSU Lightning, Environmental, Aerosol and Radar (CLEAR) framework is used to contour the 35 dBZ composite reflectivity over consecutive radar scans (Lang and Rutledge, 2011). Convective regions with a contiguous 35 dBZ composite reflectivity area are identified as new cells and tracked until merger with another cell or dissipation (Basarab et al., 2015). Flashes are then attributed to each cell if the flash initiates within or up to 10 km outside the storm cell.

To advect parcels and, therefore LNO_x contained within these parcels, dual-Doppler syntheses are performed using consecutive radar scans in each region to derive the three wind components throughout each of the storm's lifetimes. Radar fields are first gridded to 1 km in resolution for all storm domains, then radial winds are converted to U and V wind components using Radx2Grid, which converts the radar data from polar coordinates to Cartesian coordinates. NCAR CEDRIC software is then used to retrieve the vertical wind component throughout the storm volumes by integrating the mass continuity equation (Al-Momar et al., 2015). Polarimetric-based HID (Hydrometeor identification) fields were estimated for each storm using a fuzzy logic framework with CSU RadarTools (Dolan et al., 2013; Fuchs et al., 2018). Requisite thermodynamic sounding data were obtained from NWS or special DC3 soundings. The dominant hydrometeor (HID)-based fall speed is then subtracted from each grid, yielding updraft and downdraft (air) velocities. While some error is likely, this method typically resolves vertical winds inside convection to within $\pm 5 \text{ m s}^{-1}$ (Calhoun et al., 2013).

One shortfall of using multi-Doppler syntheses is that radial winds cannot be computed in areas without sufficient radar backscatter, however 3-D winds must exist outside the storm cells to allow for

parcel advection. Horizontal wind components are inferred from the NWS soundings for each vertical level to provide clear air winds surrounding the storms. Storm motion is estimated using radar trends and then subtracted from these winds so that only storm-relative winds are compared. This ensures that only storm advection is being compared among the five cases, not the environmental affects, which varied by storm. Vertical motion is set to 0 m s^{-1} for grid cells at all levels where winds cannot be determined via the dual-Doppler method. Thus, parcels that advect outside of a storm remain at that height unless the tracked storm cell encompasses the parcel again, which is more likely for parcels advected ahead of the storm. The percentages of parcels that advected outside each storm cell at the last radar scan representing the end of each storm were 81% (June 6 CO storm), 73% (June 27 CO storm), 97% (June 28 CO storm), 66% (May 18 AL storm), and 90% (June 11 AL storm). Ultimately, allowing for the advection of parcels will allow for an analysis of the final vertical distribution of LNO_x , which has important implications regarding downstream ozone production since the lifetime of NO_x increases with height.

2.3 LMA

LMA networks are constructed as a set of roughly ten stations designed to detect very high frequency (VHF) radiation emissions produced from the discontinuous breakdown of lightning channel leader propagation (Rison et al., 1999). This is seen in the form of a series of VHF sources that can vary from tens to thousands per lightning flash, depending on the spatial extent and detection efficiency of the LMA network, which is a function of network technology and flash distance from the network (Rison et al., 1999; Koshak et al., 2004; Thomas et al., 2004; Chmielewski and Bruning, 2016; Fuchs et al., 2016). One characteristic of LMA detection is an increased number of VHF sources within the positive charge region, as compared with the negative charge region, since negative leaders propagating through positive charge is a physically noisier process in the VHF portion of the spectrum, resulting in more emitted radiation (Shao and Krehbiel, 1996; Rison et al., 1999; Williams et al., 2006). Previous studies have found a mode or peak in VHF sources at temperatures $> -30^\circ\text{C}$ for anomalous thunderstorms and $< -30^\circ\text{C}$ for normal thunderstorms, thus the VHF source profile can serve as a metric for storm polarity (Wiens et al., 2005; Lang and Rutledge, 2011). Though some flash

channel detection is lost in areas of negative charge, sensitivity tests suggest the vertical distribution of flash initiation locations and flash extent does not significantly change even when low power VHF sources are removed in negative and positive charge regions of storms for both polarities (Fuchs and Rutledge, 2018). Therefore, while some channel detection is missed, we are confident in the flash channel construction for each polarity structure even in levels or regions of negative charge.

Flash processing starts with combining VHF sources into flashes based on a flash clustering algorithm described by Bruning (2013) and Fuchs et al. (2015, 2016). Here, flashes with less than ten VHF sources in Colorado and two VHF sources in Alabama were considered noise and removed from subsequent analysis, following Fuchs et al. (2015, 2016). These thresholds were defined based on individual network sensitivity. Note that it is possible that close flashes may be incorrectly combined into one larger flash or large flashes with gaps in sources to be incorrectly broken into multiple flashes. While this would affect the flash rate and LNO_x calculations per flash, the overall distribution analysis should remain relatively independent since the overall channel length remains similar (i.e. the same number of sources, and thus, channel length occurs whether it is one large or two smaller flashes).

Recent work has enabled lightning flash (channel) extent (FE) to be mapped from source locations. For example, Koshak et al. (2014) and Carey et al. (2016) followed a connect-the-dots approach in their studies of thunderstorms using the NASA Lightning Nitrogen Oxides Model (LNOM) while Bruning and Thomas (2015) discussed methods for calculating FCL from flash area and volume. Fuchs and Rutledge (2018) developed a similar methodology where flashes are mapped onto an underlying grid using their VHF source locations. In a sense, FE is constructed as a tally of 3-D grid cells containing at least one source per flash, meaning that a portion of the flash channel must traverse a grid cell to be included in the overall sum. Therefore, we assume that if a grid cell contains at least one source, then the flash traversed the grid cell, thus allowing for LNO_x to be produced for 1 km of channel length. Parcels are then created with this amount of LNO_x . Cases were selected well within optimal detection range (~125 km) of each LMA center, to maximize source detection for all five storm cases. The 3-D FE field is also created at 1 km resolution to match the 3-D radar and wind fields. Another benefit to using this resolution is that it allowed for manageable computational time

while still capturing a sufficient component of the tortuous characteristics seen in the channels according to sensitivity tests of over 40,000 thunderstorms by Fuchs and Rutledge (2018). Thus, the final distribution of these grid cells serves as a representation of each flash, or multiple flashes when integrated over an extended period of time. However, Koshak et al. (2014) found that using a 1 km resolution may result in unacceptable errors as sub-grid scale features such as additional channels and tortuosity are ignored. Much work continues to focus on better understanding such small-scale features that are important parts of lightning flashes. Future, possibly collaborative work, accounting for these finer scale features when parameterizing LNO_x before allowing for advection is certainly an exciting forethought.

2.4 Flash extent parcel advection

Dual-Doppler-derived storm wind fields provide a convenient framework for investigating LNO_x convective transport. Parcels are created such that a flash transecting N grid cells (i.e. grid cells containing ≥ 1 flash-associated source) produces N parcels. Parcels are then advected forward in a Lagrangian framework, with an evolving 3-D wind field over time in a pseudo-convective transport model method (e.g. Marquis et al., 2008; McGee and van den Heever, 2013). Advection time steps are set to 50 s to satisfy the Courant-Friedrichs-Lewy (CFL) condition (Kalnay, 2003; Skamarock et al., 2005). With these time steps, turbulent mixing between parcels and the environment is assumed to be negligible. This likely introduces some error, but when compared to ambiguity in LNO_x production, this should be less significant. One caveat to this method is that the wind information only exists at the interval of radar scans, which is roughly five minutes. Some studies use interpolation schemes such as Marquis et al. (2008), which estimate the change in wind fields between scans. However, no interpolation scheme was used in this study due to the expansive volume surrounding each storm and number of parcels undergoing advection.

One benefit to this method is that radar-derived fields, coordinates, and distance traveled can be recorded after each time step, creating a location history for each parcel. Fig. 1 provides an example of 33 parcels comprising a single flash and their trajectories for the 6 June anomalous storm. Note that parcels are advected independently of one another, so the LNO_x contained within each parcel is

retained and final profile analysis is done at the end of each storm. Also, the effect of vertical wind shear on the dispersion of LNO_x throughout the storm can be clearly seen with parcels traveling at different speeds and in different directions throughout the depth of the storm. Though some assumptions occur with this methodology, the overall benefit is that LNO_x production occurs according to FCL and can be advected accordingly, unlike other methods that treat flashes as point VHF sources or produce LNO_x uniformly for all CG and IC flashes. It is difficult to estimate the error associated with the stated assumptions of this study, however, given the similarity of results listed in Sec. 3.5 to other LNO_x studies in terms of NO_x production per flash, we believe these assumptions are reasonable.

2.5 LNO_x calculation

Parcels are created for each flash with dimensions of 1 km matching background grid resolution. We assume that the extent of each flash matches this resolution (i.e. 1 km) and thus, LNO_x is assumed to form along 1 km of FCL within a given parcel. This ignores channel tortuosity within each grid cell, but it is assumed that averaging the FCL contained per parcel among all parcels will result in minimal impacts. That is, some channels do not fully traverse grid cells, while others curve within grid cells, producing channels longer than 1 km.

LNO_x is then produced based upon the initial pressure and FE of each parcel. DeCaria et al. (2000) used the lab findings of Wang et al. (1998) who found NO_x production to be linearly proportional to FCL at a given flash current. The resulting equation yielding NO production (in molecules m⁻¹) as a function of pressure p (in Pa) is

$$N_{NO}(p) = a + bp, \quad (1)$$

with a and b being derived from a line of best fit on a graph of pressure vs. NO_x production. We assume all flashes produce a 19 kA current based on the parameterization from Wang et al. (1998), though a range in flash currents indeed exists. For example, DeCaria et al. (2000) list a CG flash mean of 15 kA, while a U.S. mean value for all flashes may sit closer to 30 kA. A basic calculation at a given pressure suggests a more energetic flash of 36 kA produces roughly 54% more LNO_x than that of a 19 kA flash, however there are many other factors that go into the chemical production of NO_x

such as tortuosity and the number of electrical discharges. Wang et al. (1998) also state the difficulty in calculating a mean current across the U.S. Changes in the current would affect the linear fit of NO_x production versus pressure and thus the constant a and coefficient b.

We use Eqn. (1) to calculate the total number of molecules of NO produced for each parcel as

$$n_{NO}(p) = (a + bp)\bar{l}, \quad (2)$$

where $a = 0.34 \times 10^{21}$ molecules m⁻¹, $b = 1.30 \times 10^{16}$ molecules m⁻¹ Pa⁻¹, and \bar{l} is the length of each grid cell traversed by each flash (set to 1 km in this study). Using basic conversions with parcel volumes, these concentrations are then converted to moles and parts per billion (ppb) to allow for easier comparison to other research (see Sec. 3.5.1). Eqn. (2) assumes a photostationary steady state assumption in that the sum of NO and NO₂ remain largely unchanged as NO_x molecules transition between each species, thus NO initially created surrounding a flash channel will quickly balance to a sum of NO and NO₂ (Leighton, 1961; DeCaria et al., 2005; Schumann and Huntrieser, 2007). It is also assumed that NO_x concentrations are not lost via chemical reactions during the advection time period (Pickering et al., 1998). To restate the purpose of this study, it is to investigate where LNO_x is being produced and to quantify its transport so that we can draw some preliminary conclusions regarding how the production and redistribution of LNO_x may impact UT ozone production. The vertical distribution of LNO_x is especially important given the lifetime of NO_x increases with altitude (Ridley et al., 1996; Schumann and Huntrieser, 2007). For purposes of this study, it is assumed that LNO_x concentrations are uniformly distributed within each parcel.

3. Results

To analyze the effects of storm polarity on NO_x production and transport, the parcel distributions will first be compared. From there, we will investigate the initial and final distributions of LNO_x by parameterizing the appropriate LNO_x concentration into each parcel based on its initial pressure level. This will allow for an in-depth analysis into the effects thunderstorm polarity may play on NO_s production and subsequent tropospheric ozone production.

3.1 Overview of the five cases

The strongest of the five storms occurred in Weld County, CO from 2259-0017 UTC 6-7 June 2012. This storm was also the most super-cellular case in that it produced a well-defined mesocyclone and remained discrete from surrounding storms during its lifetime as it moved north-northeastward from the Denver metro area towards the Wyoming border. The intensity of this storm made this storm a popular candidate for this study so transport could be investigated under conditions of extreme vertical motion. Significant hail and rainfall accompanied this storm with maximum updraft speeds approaching 40 m s^{-1} . Most VHF sources were located near 6.0 km (-12°C), indicative of predominant mid-level positive charge and anomalous polarity, though a secondary peak also occurred near 10 km (-40°C), perhaps indicating an inverted tripole charge structure. This storm produced a total of 3737 flashes with flash rates peaking at 111 min^{-1} .

The second and third anomalous (CO) cases occurred from 2154-2254 UTC on 27 June and 2039-2159 UTC 28 June 2012. Note that these storms were slightly weaker in terms of reflectivity and vertical wind speed compared to the 6 June storm, though still supercellular in nature. For the 27 June storm, a peak in VHF sources was centered around 6 km (-8°C), with flash rates peaking at 65 min^{-1} with 723 total flashes during the analysis period. Maximum updraft speeds neared 17 m s^{-1} , while peak downdrafts neared 10 m s^{-1} . The 27 June storm featured a source mode around 6 km (-8°C) and a secondary maximum near 9 km (-33°C). Similar vertical motions occurred in this storm with maximum updraft speeds reaching 15 m s^{-1} and downdrafts nearing 11 m s^{-1} . Flash rates peaked at 28 min^{-1} with 687 total flashes.

In northern Alabama, the two normal polarity storms occurred from 2223-2256 UTC 18 May 2012 and 2018-2122 UTC 11 June 2012 as isolated cells, yet they were near larger multicell complexes. Steering flow (e.g. 500 mb winds) and 0-6 km effective bulk shear were weak, causing both storms to remain nearly stationary with a slight drift towards the southeast. The storms had peaks in VHF sources between 7-8 km (-24°C ; 18 May storm) and 8-9 km (-30°C ; 11 June storm). The overall vertical extent of VHF sources was greater with a less prominent mode than that in the Colorado cases. Maximum updraft velocities neared 10 m s^{-1} in each case with 238 total flashes for

the 18 May storm and 267 flashes for the 11 June storm. See Table 1 for a list of intensity and parcel information for each storm and Table 2 for initial flash characteristics.

3.2 Anomalous polarity cases versus normal polarity cases

The three anomalous storms in Colorado tended to be more intense compared to the normal storms in Alabama. Coinciding with the lower mode in source height was the lower mode in FE height. In fact, mean FE initiation heights were between 5-6 km for the three CO anomalous cases versus 6.5- 8 km for the AL normal storms. Fig. 2 shows a cross section taken through the 6 June anomalous storm with FE contours overlaying reflectivity and HID. Close examination reveals higher FE values around 5-6 km, as is the case for the 27 and 28 June storms (figures not shown). Similarly, Fuchs and Rutledge (2018) found a mode in FE height to be ~7 km for Colorado and ~9 km for Alabama based on a study of numerous storms. Overall, the flash rates were also significantly higher for these three anomalous storms (see Figs. 3, 6 and Table 2).

Stronger vertical motion results in enhanced vertical transport of parcels from the mid-levels of the anomalous storms. For example, Fig. 3 shows that parcels initiating between 8-12 km advect upward while those below mainly < 6 km advect downward or remain close to their initiation heights, especially during flash rate peaks. Naturally, spikes in maximum updraft and downdraft speeds also occur during these periods. This appears to allow for the transport of parcels, thus creating the void of vertically-stationary parcels from 6-12 km in the 6 June storm (Fig. 3b). Similar results (not shown) are observed for the other anomalous CO cases. Towards the end of these storms, a greater fraction of all the parcels within each storm remains within the mid-levels (6-12 km) as vertical motions weaken. Note that mean parcel initiation heights for each storm are provided in Table 2.

Stronger vertical motion and higher flash rates lead to increased transport of parcels upward in the anomalous storms. Figs. 4b, e show that a higher fraction of parcels originating within the mid-levels of the 6 June storm advect to the storm upper levels compared to the 18 May storm. Strong downward transport of parcels does not seem to occur in any of the cases. FE tends to concentrate at much lower levels near 5.5 km in the anomalous thunderstorms, which places parcels in close proximity to the (base of the) stronger updrafts compared to the normal polarity cases (see Fig. 4b, e). As will be

discussed in Sec. 3.5, this has substantial impacts on tropospheric ozone production with larger amounts of LNO_x making it into the UT where it is expected to have a longer lifetime and thus greater potential for ozone production.

3.3 Normal polarity cases versus anomalous polarity cases

The two normal polarity Alabama cases are less intense with flash rates below 10 min⁻¹ and total flash counts reaching 238 (18 May 18) and 267 (11 June). These results align with the climatological study of 4000 storm observations in Fuchs et al. (2015), who found a higher fraction of Colorado storms to have flash rates over 10 min⁻¹ compared to storms in Alabama. Parcel counts are also less than half that of the weaker 27 and 28 June anomalous CO cases, totaling only 8881 (18 May) and 6737 (11 June). Fig. 5 provides a cross sectional view with total FE contoured in black for the 18 May storm near peak intensity.

A large portion of the total FE occurs at higher altitudes in the normal storms with a parcel initiation mode near 8 km (specifically 7 km for the 18 May storm and 9 km for the 11 June storm). This can be seen for the 18 May Alabama storm in Fig. 4. Note that the horizontal axes extend to only 2500 parcels for this storm, which is one tenth that of the 6 June Colorado case. Fuchs and Rutledge (2018) similarly found a FE mode around 8 km for Alabama storms. The resemblance of flash rate and FE mode for the CO and AL storms in our study to Fuchs et al. (2015) and Fuchs and Rutledge (2018) suggest that these storms represent typical storms for each region. The reader should note that while storms possessing an anomalous polarity charge structure are possible across the U.S. Southeast, research documenting such cases indicate this is an exceedingly rare occurrence. The reader should also note that while anomalous polarity thunderstorms are oftentimes more intense in nature, featuring higher reflectivity values and vertical motions, the conclusion should not be reached that strong/severe thunderstorms are always anomalous and weaker thunderstorms are normal polarity, whether in the Southeast U.S. or in the High Plains (Carey et al., 2003). Storms were chosen to match the electrical charge structure of both regions within set of completely observed storms within the DC3 project. Due to the nature of the DC3 project and the requirements for this study, no intense supercellular storms comparable to the 6 June storm could be analyzed across Alabama. This

is a limitation that will hopefully be overcome by subsequent studies, thus increasing the number of storms analyzed across both CO and AL.

Within the extent of the observed storms in this study, vertical wind speeds are less intense for the normal storms, as Figs. 6d, e show for the 18 May case compared to Fig. 3d, e. Updraft volumes also tend to stay below 100 km^3 for these two storms, indicating less available volume for significant vertical transport of parcels (see Figs. 3 and 6 for the June 6 and 18 May storms respectively). Fig. 4a,d shows that few parcels initiating below 12 km advect to a final height above 12 km, unlike that of the anomalous cases.

A notable difference in the normal storms is that the parcels initiate at higher altitudes and undergo less upward transport. Fig. 6b shows the vertical distribution time series of the fraction of parcels remaining within 2 km of initiation height for the 18 May AL storm, with similar amounts being seen for the 11 June AL storm (not shown). Notice the larger fractions of parcels within the mid-levels compared to the 6 June CO case (Fig. 3a). Over half of the parcels originating from 6-12 km in these storms remain within 2 km of their initiation heights. This differs significantly from the anomalous cases, especially the 6 June anomalous storm. Further analysis (not shown) reveals that approximately 55% of all parcels initiate and remain above 8 km (which we define as the upper troposphere [UT]), for the 11 June AL storm and 30% for the 18 May AL storm, much more than the three anomalous storms which are approximately 25% (6 June), 10% (27 June), and 17% (28 June). Vertical advection of parcels appears to be a much larger contributor toward the final fraction of parcels within the UT for anomalous storms compared to normal storms.

3.4. Comparison between all cases

Alongside the differences in vertical motions, parcel initiation height appears to also influence the advection differences observed between the two storm polarities. In the two normal storms, the average parcel modal height is $\sim 8 \text{ km}$, versus $\sim 5.5 \text{ km}$ in the anomalous cases. Since updraft and downdraft maxima are relatively weak ($|w| \leq 10 \text{ m s}^{-1}$) near these heights in the normal cases (see Fig. 6 for 18 May storm), the abundance of parcels that initiate around 8 km tend to advect less than 2 km

in the vertical. However, parcels initiating around 6 km in the anomalous cases reside near strong updrafts, increasing the potential for upward transport (see Fig. 3 for the 6 June storm).

Several trends in vertical advection appear among all five cases. First, about half of all FE parcels for each case initiate and remain below 8 km, which can be seen in Fig. 4a, d for the 6 June anomalous and 18 May normal storms. This seems to be an artifact of (1) parcels forming at lower altitudes not getting exposed to the strong updrafts in the anomalous cases (see Fig. 3), and (2) a wider vertical spread in parcel initiation heights around 8 km in the normal cases. Second, less than 5% of parcels forming above 8 km advect below this level, showing minimal strong downward transport of LNO_x regardless of storm polarity. It is possible this results from an artifact of the dual-Doppler analysis not capturing weaker downdrafts and/or a diminished presence of scatters in these regions of the storms, but it seems this was worth mentioning. Lastly, on average, roughly half of all FE parcels end up above 8 km for each case, regardless of polarity.

On the other hand, two distinct differences appear between each structure. In the normal storms, more parcels initiate and remain above 8 km (~30% for the 18 May storm and ~55% for the 11 June storm) compared to the anomalous cases (~25% for 6 June, ~10% for 27 June, and ~17% for 28 June), which is consistent with differences in the updraft maxima occurring near this level. However, a greater fraction of parcels initiate below an altitude of 8 km yet advect above this level in the anomalous cases (20%, 35%, and 45% compared to 9% and 12% for the normal cases). Fig. 3d shows the base of the maximum updrafts around 4-6 km for the 6 June case, coinciding with the modal height in FE parcel initiation. Similar placement occurs for the 27 and 28 June anomalous storms. Parcels forming here underwent strong upward advection, easily capable of being transported to levels > 8 km. Regardless, ~50% of all parcels for each storm make it above 8 km (which we define as the UT), but from two different processes. In the anomalous storms, flash locations near strong updrafts result in nearly half of parcels being transported to the UT, while flash locations near or above 8 km results in most parcels remaining at or above 8 km in the normal storms. Interestingly, most flashes initiate within updrafts for all five cases, however more within weak vertical motion in the normal storms compared to the anomalous storms (see Table 2). Perhaps more importantly, higher flash rates

and larger FE lead to a larger net quantity of parcels entering the UT in the anomalous storms (32.0%, 46.6%, and 19.7%) compared to the normal storms (12.3% and 9.5%).

3.5. LNO_x concentrations

3.5.1. Calculations

Using FE parcels for each storm, we estimate LNO_x following Eqn. (2). Fig. 7 shows LNO_x profiles for each storm before (dashed lines) and after advection (solid lines) in both kmol (a) and ppb (b). Note that the “Advected” plots represent all parcels. LNO_x production values are listed for each storm in Table 1. Interestingly, most of the parcels and corresponding total LNO_x in each storm advected outside the storm cell by the last radar scan with composite reflectivity values ≥ 35 dBZ (80% for the 6 June storm, 72% for the 27 June storm, 97% for the 28 June storm, 62% for the 18 May storm, and 89% for the 11 June storm). This makes sense because the decaying trend is captured by the CLEAR tracking program, and thus, the storm cells are much smaller as the storms come to an end and outflow from thunderstorms reaches much farther than just the areas detected by radar with reflectivity value.

3.5.2. Anomalous polarity cases

Upward transport clearly dominates in the anomalous storms. For example, 63% (6 June), 84% (27 June), and 40% (28 June) of the advected LNO_x profiles above 8 km is contributed by parcels advected upward by ≥ 2 km compared to only 12% (18 May) and 8% (11 June; see Table 1) in the normal storms. The “Advected” profiles for the 6 and 27 June anomalous storms are nearly a reversal of the original profiles prior to advection, where parcel heights transition from unimodal to bimodal distributions. For example, Fig. 7c shows that enhanced vertical motions transport a significant portion of parcels above 8 km in the three anomalous cases. This makes sense considering Fig. 8 shows that these two storms produce the most LNO_x parcels, which also initiate within/near stronger vertical winds. In addition, updraft volumes ($w \geq 5 \text{ m s}^{-1}$) are much larger ($\sim 800 \text{ km}^3$ for the 6 June storm and $\sim 400 \text{ km}^3$ for the 27 June storm), and remain consistently larger throughout the storm

lifetimes compared to updraft volumes generally below 150 and 300 km³ for the 18 May and 11 June normal polarity storms (see Figs. 3d, 6d). Note that the mixing ratios above 8 km in Fig. 7b appear larger than the concentration profiles in Fig. 7a because pressure and air density are lower at these altitudes, which lower LNO_x production as given in Eqn. (2). Vertical transport for the anomalous storms is comparable to Ott et al. (2010), who found enhanced LNO_x mass fractions above 8 km for modeled mid-latitude storms, though less defined than what is observed for these three cases.

These results suggest that the enhanced updraft strength and width, which Fuchs et al. (2015) found to be characteristic of anomalous storms, helps to transport LNO_x to the UT. On average, 14% of all parcels originate in updrafts $\geq 5 \text{ m s}^{-1}$ in these storms compared to 7% in normal polarity cases. This is exemplified in Fig. 7c where the vertical profiles of LNO_x contributed to by upward, downward, or neutral advection are normalized by the total LNO_x production in the corresponding storm. A larger fraction of LNO_x above 8 km in the anomalous storms is contributed to by upward-advected parcels marked by the red curves. While a smaller fraction of parcels originates in strong updrafts, as seen in Fig. 4 and 8, the proximity of parcels to the updraft cores of the anomalous storms allows for this deep upward advection.

LNO_x concentration and mixing ratio profiles change less for the normal storms. There is LNO_x enhancement from 10-12 km evident in Fig. 7a, though less than that in the anomalous cases. Ott et al. (2010) found similar “C-shaped” vertical LNO_x mass fractions with a single mode also around 8 km for modeled storms in the subtropics. While the proportion of parcels ending above 8 km is still around 50% in these two normal storms, the contributions to UT LNO_x appears to be driven more so by higher initial FE in these thunderstorms than by vertical advection, which is in stark contrast to the anomalous cases. For example, Fig. 7c shows a larger portion of LNO_x above 8 km is produced within parcels that remain above this height throughout the lifetime of the storm. LNO_x transport to the UT appears to result from two different processes – advection-driven distribution in the anomalous storms, and location-driven distribution in the normal thunderstorms.

3.5.3 LNO_x within the boundary layer

Results from this study also suggest that an appreciable portion of the LNO_x produced within anomalous thunderstorms may end up within the BL. Pollack et al. (2016) note that previous studies (i.e. Chameides et al., 1987; Skamarock et al., 2003) assume little to no LNO_x enters the BL and therefore disregarded this process, appearing to miss an appreciable LNO_x transport pathway. For example, Figs. 7a, b show that an appreciable amount of LNO_x exists in the lowest levels of the anomalous cases after parcels have undergone advection. In fact, further investigation shows that approximately 16% (June 6), 44% (June 27), 65% (June 28), 3.0% (May 18), and 0.1% (June 11) of the total LNO_x produced from each storm ends up in the BL (BL heights listed in Table 1). Contrary to previous assumptions, this is a significant fraction of the total LNO_x for the anomalous cases. Future work is required to confirm that anomalous storms transport an appreciable fraction of their total LNO_x to the BL, however Fig. 7c shows clear peaks in the black curve for each of these three cases, meaning that parcels remaining relatively stationary (within 2 km of initial heights) contribute the bulk of the LNO_x within the BL. Therefore, according to these trajectory analyses, nearly all the LNO_x at the lowest levels of these storms results from parcels that remain close to their initial heights. This also appears to be the case for the two normal polarity cases, though less LNO_x appears to reside in lower levels of these storms due to the higher flash channel modal height. The purple curves suggest that strong downward transport of LNO_x via parcels does not seem to occur in any of the five cases, regardless of polarity. Examining the positioning of updrafts in the anomalous storms in Fig. 3 shows that maximum updrafts occur within cloud level and above the lifting condensation level (LCL) for each of these storms (see Table 1 for LCLs). The overall lower mode in flash channel (parcel) initiation within the three anomalous storms appears to position a large fraction of parcels directly beneath the strongest updraft cores, allowing for deep upward advection of some parcels, while others remain too low to be transported. On the other hand, most flash channels occur above the shallower BLs in the two normal storms, thus preventing appreciable LNO_x concentrations within their BLs.

As was previously mentioned, due to the set of storms that occurred during DC3 and the criteria necessary for thorough observation, analysis of an intense, normal polarity supercell over Alabama was not possible. This poses the question as to whether the LNO_x characteristics of the two normal polarity storms is more a result of the location of the lightning channels/LNO_x formation or whether it is due to the placement of the LNO_x above the strongest updrafts? It is likely a combination of both given the similarity of the observed flash extent to that seen in Fuchs and Rutledge (2018) and the fact that the LNO_x profiles are similar to those discussed in Ott et al. (2010). Future studies may help to answer this question.

3.5.4 Individual flash estimates and aircraft measurements

During DC3, the NASA DC-8 research aircraft measured various inflow concentrations while the National Science Foundation (NSF)/National Center for Atmospheric Research (NCAR) Gulfstream-V (G-V) aircraft measured outflow concentrations of 17 different thunderstorm anvils. Subtracting the inflow from outflow NO_x values allows for total LNO_x to be estimated (Schuman and Huntrieser, 2007; Pollack et al., 2016). Unfortunately, weak environmental winds in the AL storms led to diminished outflow in one direction necessary for aircraft measurement and increased likelihood of under-representative LNO_x measurements, so no useable observations exist (Pollack et al., 2016).

Following Eqn. (2) and using reconstructed FE, we estimate slightly lower LNO_x production per flash compared to select previous studies. For each storm, we compute an average production of 72 moles NO_x fl⁻¹ (6 June), 158 moles fl⁻¹ (27 June), 143 moles fl⁻¹ (28 June), 92 moles fl⁻¹ (18 May), and 61 moles fl⁻¹ (11 June). Pollack et al. (2016) estimate 60-570 moles of LNO_x fl⁻¹ for a subset of DC3 storms using a mesoscale flux and volume approach, in contrast to the FE method used in our study. In another study, Barthe and Barth (2008) estimate $\sim 121 \pm 41$ moles fl⁻¹ for a simulated STERAO storm characterized by high cloud base and high shear, similar to our anomalous cases. Simulating the same STERAO storm as Barthe and Barth (2008), Ott et al. (2010) estimated 240 moles fl⁻¹. In their summary article, Schumann and Huntrieser (2007) report a global average production of 250 moles fl⁻¹, with a range of 32-664 moles fl⁻¹.

Research suggests stronger electric fields build during peaks in storm intensity (associated with charge layers being in closer proximity to one another) resulting in physically shorter flashes (e.g. Carey et al., 2005; Kuhlman et al., 2009; Weiss et al., 2012; Bruning and MacGorman, 2013; Mecikalski et al., 2015). Additional investigation into these five storms (not shown) presents similar results with reduced total FE during periods of higher flash rate ($r^2 \cong 0.7$ for all five storms). It should be noted that when total LNO_x production is divided into the number of flashes for each storm, as was done by Pollack et al. (2016), FE and LNO_x production are inherently assumed to be equal among all flashes. However, our results show that FE and LNO_x are quite variable (see LNO_x range and standard deviation per flash for each storm in Table 1).

Since DC3 aircraft observations are available for the 6 June storm, LNO_x production from a flux-based approach can be estimated like the method discussed in Pollack et al. (2016). To do so, a net LNO_x production time series is computed by subtracting ambient, measured NO_x inflow from the NASA DC8 ten minutes prior to real-time measured NO_x by the G-V aircraft in the storm anvil outflow. Thus, the net NO_x production calculated is assumed to be solely attributed to lightning and can then be divided by the number of flashes that also occurred within the corresponding ten minutes to generate a LNO_x production time series. Results from this time series suggest a mean LNO_x production of ~ 190 moles fl⁻¹, with a maximum of ~ 2300 moles fl⁻¹. This is comparable to Pollack et al. (2016) and much larger than the mean calculated via the parcel method for this storm, 72 moles fl⁻¹. This suggests that flux/volume approaches, which inherently assume equal production among all flashes, may overlook the higher frequency of shorter flashes that often occur during higher storm intensity and flash rate periods. Doing so may overestimate the average individual flash LNO_x estimate. This idea is not new as Skamarock et al. (2003) also found a lower average flash estimate of 43.2 moles fl⁻¹ in a similar method where LNO_x observations were compared to observed flash rate and derived FCL from a lightning interferometer. Carey et al. (2016) came to similar conclusions in finding storm intensity properties such as graupel volume/mass, updraft volume, max updraft speed, etc. to be more closely related to flash rate than extent, suggesting that more intense storms do not always result in increased channel length. Similarly, Mecikalski and Carey (2018b) found mean flash size to decrease from multicell, to mesoscale convective system, to supercell thunderstorms, further

suggesting a relationship exists between shorter flash length and storm intensity. It remains unclear as to whether this tendency exists for only IC flashes, CG flashes, or both, however, this topic is beyond the scope of this study. The decrease in flash channel length during storm intensification may counter the notion that IC and CG flashes produce similar amounts of LNO_x.

4. Conclusions

Over 5000 flashes totaling over 206,500 km of LMA-observed FE are divided into 1.0 km parcels for five DC3 thunderstorms to investigate LNO_x production and distribution within normal and anomalous polarity thunderstorms. Averaging LNO_x production across all observed flashes separately for each of the five storms produces a single flash estimate in accord with previous estimates of 61-158 moles fl⁻¹, though this sits on the lower end of other recent estimates. We hypothesize this to result from an increased number of shorter flashes occurring during the higher flash rate periods for each storm, though future research is needed to confirm this. On the other hand, many previous studies also observed flash counts via other methods such as the NASA Lightning Imaging Sensor (LIS), whereas LMA networks tend to have higher flash detection efficiencies than satellite observations such as LIS (Fuchs et al., 2016). There is also uncertainty in this estimate based on the flash current used, as higher currents would increase these estimates, but uncertainty in the mean current for each storm proves challenging. Future work expanding on the number of storm cases within each region, possibly considering flash current will likely draw interesting conclusions on LNO_x production and transport tendencies across both regions.

Readers should note that environmental conditions such as elevated CAPE, moisture content, etc. play an important role in developing charge structures within each storm, thus it is not just its location (e.g Colorado or Alabama). Thunderstorms for this study were chosen to best match the climatological normal for each region following Fuchs and Rutledge (2018). A variety of these environmental conditions are listed for each storm in Table 1. The reader should also note that the five storms chosen in this study were chosen to best match the observed electrical charge structure native to both CO and AL. Varying degrees of storm intensity and charge structure are possible over both regions. Moreover, this study does not imply that anomalous storms are always more intense than

normal polarity storms; oftentimes, intense storms over the High Plains are anomalous, but intense normal polarity storms are also common over the Southeastern U.S. and elsewhere. Future work investigating more storms over both regions will only help to strengthen the conclusions reached in this study.

Results show FE modal height is lower in the anomalous storms (~5.5 km) than in the normal storms (~8 km). Like previous research, our results show enhanced updrafts with larger continuous updraft volumes $\geq 5 \text{ m s}^{-1}$ also occur within anomalous storms. Though FE is lower in initial altitude, more parcels advect upward $\geq 2 \text{ km}$ (~70%) compared to the normal storms (~35%), resulting in greater LNO_x advection upward to the UT, as can be seen in Fig. 7. Between all five storms, most FCL originated in weak updrafts ($5 \text{ m s}^{-1} \geq |w|$), yet within proximity to strong updrafts greater than 5 m s^{-1} , especially for the anomalous storms. However, a greater portion of the remaining FCL occurs in the strong updrafts in these storms compared to normal storms. Thus, higher flash rates and increased updraft strength collectively work to increase LNO_x concentrations within the UT, overcoming the lower height at which LNO_x is produced. Since NO_x lifetime increases with height, more LNO_x -induced ozone production is likely to occur in residual anvil outflow following these anomalous storms. This suggests that anomalous storms may have greater downstream ozone production, though investigation of more cases will help to substantiate these claims. However, though not completely understood, it is estimated that only a small fraction of global thunderstorms possesses an anomalous charge structure, thus the global impact of increased LNO_x transport to the UT from these storms may be less significant.

Attention must be paid to the vertical profile of FCL used to parameterize LNO_x within the model domain; profiles with a top-heavy bias may overestimate ozone production and profiles with a bottom-heavy bias may underestimate production. We have only investigated five storms, representing two different storm environments. Future work investigating lightning characteristics of differing environments, including more thunderstorms within the High Plains and U.S. Southeast, as well as different convective modes of thunderstorms would greatly benefit modeling studies investigating LNO_x and ozone production over various regions of the globe. Developing average

FE/FCL profiles and single flash production estimates is one way this can be done. Using these results alongside future work may improve LNO_x production accuracy at the local and, perhaps, global level.

Acknowledgements

The authors thank Brett Basarab for data used in the Colorado anomalous storm cases, Paul Hein (CSU) for technical assistance provided, and Brenda Dolan (CSU) for radar processing assistance.

The authors also thank Emily Fischer and Ilana Pollack (CSU) for providing insightful discussion on NO_x-related tropospheric chemistry as well as Mary Barth (NCAR) for providing helpful discussion on DC3 research and LNO_x modeling. The COLMA network, data, and processing are managed by Paul Krehbiel, William Rison, and Ronald Thomas at New Mexico Tech. The NALMA network and data are provided by the National Aeronautics and Space Administration (NASA) Marshall Space Flight Center (MSFC), while processing is provided by the University of Alabama at Huntsville in cooperation with NASA MSFC. Visit <https://github.com/deeplycloudy/lmatools> for more information regarding the flash clustering algorithm used to create flashes for this study. Data used for this study can be obtained on the DC3 webpage: https://data.eol.ucar.edu/master_list/?project=DC3. Sounding data was retrieved from the University of Wyoming Department of Atmospheric Science. Funding for this study was provided by NSF PDM grant number AGS-1429925. Much appreciation is extended to the reviewers of this article; their insight led to substantial improvements. The authors acknowledge and thank everyone involved with DC3 project for helping make this study possible.

References

- Al-Momar, S., Deierling, W., Williams, J.K. (2015), Examining in-cloud convective turbulence in relation to total lightning and the 3D wind field of severe thunderstorms, 17th Conf. on Aviation, Range, and Aerospace Meteorology, Phoenix, AZ, Amer. Meteor. Soc., 5.3.
- Apel, E. C., and co-authors (2015), Upper tropospheric ozone production from lightning NO_x-impacted convection: Smoke ingestion case study from the DC3 campaign, J. Geophys. Res. Atmos., 120, 2505–2523.

Bain, A. L., R. Matthee, and L. Carey (2013), Polarimetric radar and electrical observations of deep moist convection across northern Alabama during the DC3 Experiment, 4A.5, AMS 36th Conference on Radar Meteorology, Breckenridge, CO, September 16-20,

2013, <https://ams.confex.com/ams/36Radar/webprogram/Paper228662.html>.

Bain, A. L. (2013) "Polarimetric Doppler Radar and Electrical Observations of Deep Moist Convection across Northern Alabama during the Deep Convective Clouds and Chemistry Experiment", Master's Thesis, The University of Alabama in Huntsville, 148 pp. https://www.nsstc.uah.edu/armor/publications/Bain_thesis.pdf.

Barthe, C., and M. C. Barth (2008), Evaluation of a new lightning-produced NO_x parameterization for cloud resolving models and its associated uncertainties, *Atmos. Chem. Phys.*, 8, 4691–4710.

Barth, M.C., and co-authors (2015), The Deep Convective Clouds and Chemistry (DC3) field campaign, *Bull. Amer. Meteor. Soc.*, 96, 1281–1309.

Basarab, B. M., S. A. Rutledge, and B. R. Fuchs (2015), An improved lightning flash rate parameterization developed from Colorado DC3 thunderstorm data for use in cloud-resolving chemical transport models, *J. Geophys. Res. Atmos.*, 120 (18), 9481–9499.

Boccippio, D.L., K.L. Cummins, H.J. Christian, and S.J. Goodman (2001), Combined satellite- and surface-based estimation of the intracloud-cloud-to-ground lightning ratio over the continental United States. *Mon. Wea. Rev.*, 129, 108-122.

Bruning, E. C. and D. R. MacGorman (2013), Theory and observations of controls on lightning flash size spectra, *J. Atmos. Sci.*, 70, 4012–4029.

Bruning, E. C. (2013), Streamed clustering of lightning mapping data in Python using sklearn, in *Proceedings 12th Python in Science Conference (SciPy)*, vol. 2, Austin, Tex.

Bruning, E. C., and R. J. Thomas (2015), Lightning channel length and flash energy determined from moments of the flash area distribution, *J. Geophys. Res.: Atmos.*, 120, 8925-8940.

Bruning, E., S. A. Weiss, and K. M. Calhoun (2014), Continuous variability in thunderstorm primary electrification and an evaluation of inverted-polarity terminology, *Atmos. Res.*, 135, 274-284.

Buffen, A. M., M. G. Hastings, L. G. Thompson, and E. Mosley-Thompson (2014), Investigating the preservation of nitrate isotopic composition in a tropical ice core from the Quelccaya Ice Cap, Peru, *J. Geophys. Res. Atmos.*, 119, 2674–2697.

Calhoun, K.M., D.R. MacGorman, C.L. Ziegler, and M.I. Biggerstaff (2013), Evolution of Lightning Activity and Storm Charge Relative to Dual-Doppler Analysis of a High-Precipitation Supercell Storm, *Mon. Wea. Rev.*, 141, 2199–2223.

Carey, L. D., S. A. Rutledge and W. A. Petersen, 2003: The relationship between severe storm reports and cloud-to-ground polarity in the contiguous United States from 1989-1998. *Mon. Wea. Rev.*, 131, 1211-1228.

Carey, L.D. and K.M. Buffalo (2007), Environmental control of cloud-to-ground lightning polarity in severe storms, *Mon. Wea. Rev.*, 135, 1327–1353.

Carey, L. D., Koshak, W., Peterson, H., and Mecikalski, R. M. (2016), The kinematic and microphysical control of lightning rate, extent, and NO_x production, *J. Geophys. Res. Atmos.*, 121, 7975– 7989.

Carey, L. D., M. J. Murphy, T. L. McCormick, and N. W. Demetriades (2005), Lightning location relative to storm structure in a leading-line trailing stratiform mesoscale convective system, *J. Geophys. Res.*, 110, D03105.

Cecil, D. J., D. E. Buechler, and R. J. Blakeslee (2014), Gridded lightning climatology from TRMM-LIS and OTD: Dataset description, *Atmospheric Research*, 135, 404-414.

Chameides, W. L., D. D. Davis, J. Bradshaw, M. Rodgers, S. Sandholm, and D. B. Bai (1987), An estimate of the NO_x production-rate in electrified clouds based on NO observations from the GTE/CITE-1 fall 1983 field operation, *J. Geophys. Res.*, 92, 2153–2156.

Chmielewski, V. C., and E. C. Bruning (2016), Lightning mapping array flash detection performance with variable receiver thresholds, *J. Geophys. Res. Atmos.*, 121 (14), 8600-8614.

Christian, H. J., R. J. Blakeslee, S. J. Goodman, D. Boccippio, and coauthors (2003), Global frequency and distribution of lightning as observed from space by the Optical Transient Detector, *J. Geophys. Res.*, 108, 4-15.

DeCaria, A. J., K. E. Pickering, G. L. Stenchikov, J. R. Scala, J. L. Stith, J. E. Dye, B. A. Ridley, and P. Laroche (2000), A cloud-scale model study of lightning-generated NO_x in an individual thunderstorm during STERAO-A, *J. Geophys. Res.*, 105, 11.

DeCaria, A. J., K. E. Pickering, G. L. Stenchikov, and L. E. Ott (2005), Lightning-generated NO_x and its impact on tropospheric ozone production: A three-dimensional modeling study of a Stratosphere-Troposphere Experiment: Radiation, Aerosols and Ozone (STERAO-A) thunderstorm, *J. Geophys. Res. Atmos.*, 110 (D14).

Deierling, W., and W. A. Petersen (2008), Total lightning activity as an indicator of updraft characteristics, *J. Geophys. Res.*, 106, 20,395-20,402.

Dolan, B., S. A. Rutledge, S. Lim, V. Chandrasekar, and M. Thurai (2013), A robust C-band hydrometeor identification algorithm and application to a long-term polarimetric radar dataset, *J. Appl. Meteor. Climatol.*, 52 (9), 2162-2186.

Dye, J.E., et al. (2000), An overview of the Stratospheric-Tropospheric Experiment: Radiation, Aerosols, and Ozone (STERAO)-Deep Convection experiment with results for the July 10, 1996 storm, *J. Geophys. Res.*, 105 (D8), 10,023-10,045.

Fehr, T., H. Höller, and H. Huntrieser (2004), Model study on production and transport of lightning-produced NO_x in a EULINOX supercell storm, *J. Geophys. Res.*, 109, 1-17.

Fuchs, B. R., E. C. Bruning, S. A. Rutledge, L. D. Carey, P. R. Krehbiel, and W. Rison (2016), Climatological analyses of LMA data with an open-source lightning flash-clustering algorithm, *J. Geophys. Res. Atmos.*, 121 (14), 8625-8648.

Fuchs, B. R., S. A. Rutledge, B. Dolan, L. D. Carey, C. Schultz (2018), Microphysical and kinematic processes associated with anomalous charge structures in isolated convection, *J. Geophys. Res. Atmos.*, 123, 6505–6528.

Fuchs, B. R., S. A. Rutledge, E. C. Bruning, J. R. Pierce, J. K. Kodros, T. J. Lang, D. R. MacGorman, P. R. Krehbiel, and W. Rison (2015), Environmental controls on storm intensity and charge structure in multiple regions of the continental United States, *J. Geophys. Res. Atmos.*, 120 (13), 6575-6596.

Fuchs, B. R., and S. A. Rutledge (2018), Investigation of lightning flash locations in isolated convection using LMA observations, *J. Geophys. Res. Atmos.*, 123, 6158-6174.

Hansen, A. E., Fuelberg, H. E., and Pickering, K. E. (2010), Vertical distributions of lightning sources and flashes over Kennedy Space Center, Florida, *J. Geophys. Res.*, 115, D14203.

Huntrieser, H., and coauthors (2016), Injection of lightning-produced NO_x , water vapor, wildfire emissions, and stratospheric air to the UT/LS as observed from DC3 measurements, *J. Geophys. Res. Atmos.*, 121, 6638–6668.

Jayarathne, E. R., and Saunders, C. P. R. (1983), Charge on ice crystals in laboratory clouds, *J. Geophys. Res.*, 88(C9), 5494–5496.

Kalnay, E. (2003), Atmospheric modeling, data assimilation, and predictability, 73-90 pp., Cambridge Univ. Press, New York.

Koshak, W., H. Peterson, A. Biazar, M. Khan, and L. Wang (2014), The NASA Lightning Nitrogen Oxides Model (LNOM): Application to air quality modeling. *Atmos. Res.*, 135-136, 363-369.

Koshak, W. J., and co-authors (2004), North Alabama lightning mapping array (LMA): VHF source retrieval algorithm and error analyses. *J. Atmos. Oceanic Technol.*, 21(4), 543-558.

- Krehbiel, P., R. J. Thomas, W. Rison, T. Hamlin, M. Davis, and J. Harlin (2000), Lightning mapping observations in central Oklahoma, *Eos*, 81 (3), 21-25.
- Kuhlman, K. M., D. R. MacGorman, M. I. Biggerstaff, and P. R. Krehbiel (2009), Lightning initiation in the anvils of two supercell storms, *Geophys. Res. Lett.*, 36, L07802.
- Labrador, L. J., R. von Kuhlmann, and M. G. Lawrence (2005), The effects of lightning-produced NO_x and its vertical distribution on atmospheric chemistry: Sensitivity simulations with MATCH-MPIC, *Atmos. Chem. Phys.*, 5, 1815-1834.
- Lang, T. J., S. A. Rutledge, J. E. Dye, M. Venticinque, P. Laroche, and E. Defer (2000), Anomalous low negative cloud-to-ground lightning flash rates in intense convective storms observed during STERAO-A. *Mon. Wea. Rev.*, 128, 160–173.
- Lang, T. J., S. A. Rutledge, and K. C. Wiens (2004), Origins of positive cloud-to-ground lightning flashes in the stratiform region of a mesoscale convective system, *Geophys. Res. Lett.*, 31, L10105.
- Lang, T. J., and S. A. Rutledge (2011), A framework for the statistical analysis of large radar and lightning datasets: Results from STEPS 2000, *Mon. Wea. Rev.*, 139, 2536-2551.
- Lawrence, M. G., W. L. Chameides, P. S. Kasibhatla, H. Levy II, and W. Moxim (1995), Lightning and Atmospheric Chemistry: The Rate of Atmospheric NO Production, vol. I, pp. 189–202, CRC Press, Boca Raton, Fla.
- Leighton, P. A. (1961), *Photochemistry of air pollution*, 300 pp., Elsevier, New York.
- Levy II, H., W. J. Moxim, and P. S. Kasibhatla (1996), A global three-dimensional time-dependent lightning source of tropospheric NO_x , *J. Geophys. Res.*, 101(D17), 22,911–22,922.
- MacGorman, D. R., and W. D. Rust (1998), *The Electrical Nature of Storms*, 422 pp., Oxford Univ. Press, New York.
- MacGorman, D. R., et al. (2008), TELEX the thunderstorm electrification and lightning experiment, *Bull. Am. Meteorol. Soc.*, 89, 997–1013.

Maggio, C., L. Coleman, T. Marshall, M. Stolzenburg, M. Stanley, T. Hamlin, P. Krehbiel, W. Rison, and R. Thomas (2005), Lightning-initiation locations as a remote sensing tool of large thunderstorm electric field vectors, *J. Atmos. Oceanic Technol.*, 22 (7), 1059-1068.

Makowski, J. A., D. R. MacGorman, M.I. Biggerstaff, and W.H. Beasley, 2013: Total lightning characteristics relative to radar and satellite observations of Oklahoma mesoscale convective systems, *Mon. Wea. Rev.*, 141, 1593–1611.

Mecikalski, R. M., A. L. Bain, and L. D. Carey (2015), Radar and lightning observations of deep moist convection across northern Alabama during DC3: 21 May 2012, *Mon. Wea. Rev.*, 143(7), 2774–2794.

Mecikalski, R. M., and L. D. Carey (2017), Lightning characteristics relative to radar, altitude and temperature for a multicell, MCS, and supercell over northern Alabama. *Atmos. Res.*, 191, 128-140.

Mecikalski, R. M., and L. D. Carey (2018a), Radar reflectivity and altitude distributions of lightning flashes as a function of three main storm types. *J. Geophys. Res. Atmos.*, 123, 12,814-12,828.

Mecikalski, R. M., and L. D. Carey (2018b), Radar reflectivity and altitude distributions of lightning as a function of IC, CG and HY flashes: Implications for LNO_x production. *J. Geophys. Res. Atmos.*, 123, 12,796-12,813.

Mecikalski, R. M., P. M. Bitzer, and L. D. Carey (2017), Why flash type matters: A statistical analysis. *Geophys. Res. Lett.*, 44, 9505-9512.

Nault, B. A., J. L. Laughner, P. J. Wooldridge, J. D. Crounse, J. Dibb, G. Diskin, J. Peischl, J. R. Podolske, I. B. Pollack, T. B. Ryerson, E. Scheuer, P. O. Wennberg, and R. C. Cohen (2017), Lightning NO_x emissions: Reconciling measured and modeled estimates with updated NO_x chemistry, *Geophys. Res. Lett.*, 44, 9479–9488.

Nelson, S. P., and R. A. Brown (1987), Error sources and accuracy of vertical velocities computed from multiple-Doppler radar measurements in deep convective storms, *J. Atmos. Oceanic Technol.*, 4, 233–238.

Ott, L. E., K. E. Pickering, G. L. Stenchikov, D. J. Allen, A. J. DeCaria, B. Ridley, R.-F. Lin, S. Lang, and W.-K. Tao (2010), Production of lightning NO_x and its vertical distribution calculated from three-dimensional cloud-scale chemical transport model simulations. *J. Geophys. Res.*, 115, D04301.

Ott, L. E., K. E. Pickering, G. L. Stenchikov, H. Huntrieser, and U. Schumann (2007), Effects of lightning NO_x production during the 21 July European Lightning Nitrogen Oxides Project storm studied with a three dimensional cloud-scale chemical transport model, *J. Geophys. Res.*, 112, D05307.

Pickering, K. E., Y. Wang, W.-K. Tao, C. Price, and J.-F. Muller (1998), Vertical distributions of lightning NO_x for use in regional and global chemical transport models, *J. Geophys. Res.*, 103(D23), 31,203–31,216.

Pollack, I. B., C. R. Homeyer, T. B. Ryerson, K. C. Aikin, J. Peischl, E. C. Apel, T. Campos, F. Flocke, R. S. Hornbrook, D. J. Knapp, et al. (2016), Airborne quantification of upper tropospheric NO_x production from lightning in deep convective storms over the United States Great Plains, *J. Geophys. Res. Atmos.*, 121, 2002–2028.

Price, C., and D. Rind (1992), A simple lightning parameterization for calculating global lightning distributions, *J. Geophys. Res.*, 97(D9), 9919–9933.

Price, C., J. Penner, and M. Prather (1997), NO_x from lightning: 1. Global distribution based on lightning physics, *J. Geophys. Res. Atmos.*, 102 (D5), 5929–5941.

Reap, R. M., and D. R. MacGorman (1989), Cloud-to-Ground Lightning: Climatological characteristics and relationships to model fields, radar observations, and severe local storms, *Mon. Wea. Rev.*, 117, 518–535.

Ridley, B. A., J. E. Dye, J. G. Walega, J. Zheng, F. E. Grahek, and W. Rison (1996), On the production of active nitrogen by thunderstorms over New Mexico. *J. Geophys. Res.*, 101 (D15), 20,985–21,005.

Ridley, B. A., K. E. Pickering, and J. E. Dye (2005), Comments on the parameterization of lightning-produced NO in global chemistry-transport models. *Atmospheric Environment*, 39, 6184-6187.

Rison, W., R. Thomas, P. Krehbiel, T. Hamlin, and J. Harlin (1999), A GPS-based three-dimensional lightning mapping system: Initial observations in central New Mexico, *Geophys. Res. Lett.*, 26, 3573-3576.

Rust, W. D., D. R. MacGorman, E. C. Bruning, S. A. Weiss, P. R. Krehbiel, R. J. Thomas, W. Rison, T. Hamlin, and J. Harlin (2005), Inverted-polarity electrical structures in thunderstorms in the Severe Thunderstorm Electrification and Precipitation Study (STEPS), *Atmos. Res.*, 76, 247-271.

Rutledge, S. A. and D. R. MacGorman (1988), Cloud-to-ground lightning activity in the 10–11 June 1985 mesoscale convective system observed during the Oklahoma–Kansas PRE-STORM project, *Mon. Wea. Rev.*, 116, 1393–1408.

Saunders, C. P. R., and S. L. Peck (1998), Laboratory studies of the influence of the rime accretion rate on charge transfer during crystal/graupel collisions, *J. Geophys. Res.*, 103 (D12). 13,949–13,956.

Saunders, C. P. R., W. D. Keith, and R. P. Mitzeva (1991), The effect of liquid water on thunderstorm charging, *J. Geophys. Res.*, 96, 11,007-11,017.

Schumann, U., and H. Huntrieser (2007), The global lightning-induced nitrogen oxides source, *Atmos. Chem. Phys.*, 7 (14), 3823-3907.

Shao, X. M., and P. R. Krehbiel (1996), The spatial and temporal development of intracloud lightning, *J. Geophys. Res.*, 101(D21), 26641–26668.

Skamarock, W. C., J. B. Klemp, J. Dudhia, D. O. Gill, D. M. Barker, W. Wang, and J. G. Powers (2005), A description of the Advanced Research WRF Version 2, NCAR Technical Note, 21-22.

Skamarock, W. C., J. E. Dye, E. Defer, M. C. Barth, J. L. Stith, B. A. Ridley, and K. Baumann (2003), Observational- and modeling-based budget of lightning-produced NO_x in a continental thunderstorm, *J. Geophys. Res.*, 108 (D10), 4305.

Stith, J., J. Dye, B. Ridley, P. Laroche, E. Defer, K. Baumann, G. Hübler, R. Zerr, and M. Venticinque (1999), NO signatures from lightning flashes, *J. Geophys. Res.*, 104 (D13), 16081–16089.

Takahashi, H., K. Suzuki, and G. Stephens (2017), Land-ocean differences in the warm-rain formation process in satellite and ground-based observations and model simulations, *Q. J. R. Meteorol. Soc.*, 143 (705), 1804-1815.

Takahashi, T. (1978), Riming electrification as a charge generation mechanism in thunderstorms, *Atmos. Sci.*, 35, 1536-1548.

Tessendorf, S. A., S. A. Rutledge, and K. C. Wiens (2007), Radar and lightning observations of normal and inverted multicellular storms from STEPS, *Mon. Wea. Rev.*, 135, 3682-3706.

Thomas, R. J., P. R. Krehbiel, W. Rison, S. J. Hunyady, W. P. Winn, T. Hamlin, and J. Harlin (2004), Accuracy of the lightning mapping array, *J. Geophys. Res.*, 109, 14 207-14 216.

Wang, Y., A. W. DeSilva, G. C. Goldenbaum, and R. R. Dickerson (1998), Nitric oxide production by simulated lightning: Dependence on current, energy and pressure, *J. Geophys. Res.*, 103, 19,149–19,159.

Weiss, S. A., D. R. MacGorman, and K. M. Calhoun (2012), Lightning in the anvils of supercell thunderstorms, *Mon. Wea. Rev.*, 140, 2064-2079.

Wiens, K. C., S. A. Rutledge, and S. A. Tessendorf (2005), The 29 June 2000 supercell observed during STEPS Part II: Lightning and charge structure, *J. Atmos. Sci.*, 62, 4151–4177.

Williams, E. R., V. Mushtak, D. Rosenfeld, S. Goodman, and D. Boccippio (2005), Thermodynamic conditions favorable to superlative thunderstorm updraft, mixed phase microphysics and lightning flash rate, *Atmos. Res.*, 76, 288–306.

Williams, E. R. (2006), Problems in lightning physics: The role of polarity asymmetry, *Plasma Sources Sci. Technol.*, 15 (2), S91.

Williams, E. R. (1989), The tripole structure of thunderstorms. *J. Geophys. Res.*, 94, 13,151-13,167.

Wu, S., L. J. Mickley, D. J. Jacob, J. A. Logan, R. M. Yantosca, and D. Rind (2007), Why are there large differences between models in global budgets of tropospheric ozone?, *J. Geophys. Res.*, 112, D05302.

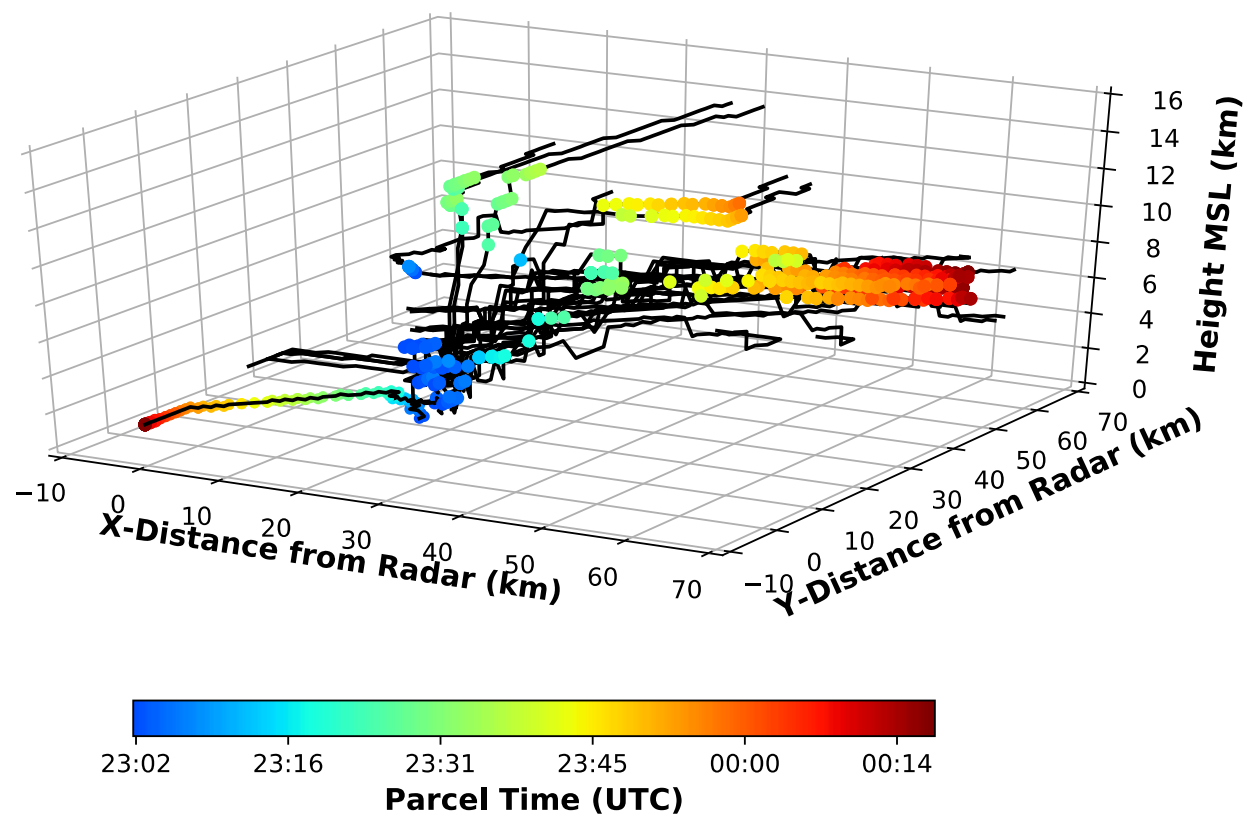


Figure 1: Example trajectories of individual flash extent (FE) parcels initialized for a single flash in the June 6, 2012 Colorado storm. Parcels are initialized at their respective starting location and advected forward following dual-Doppler derived winds. Trajectories are colored by time from the initial flash time (blue) to the storm's ending time (red). Note the flash displayed is comprised of 33 parcels with 101 time steps. Notice the varying directions and velocity in which parcels advect due to changes in wind speed and direction with height.

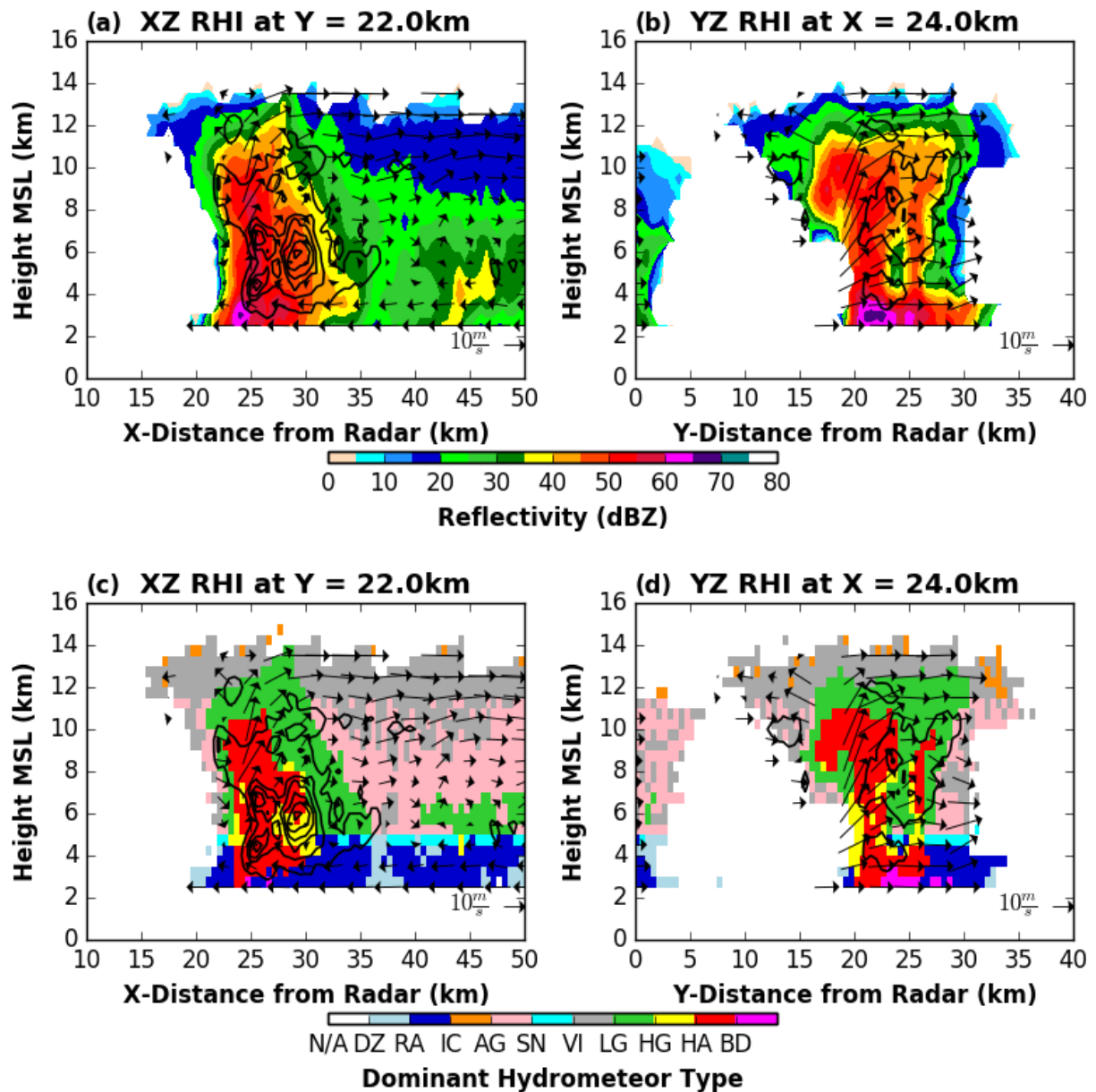


Figure 2: Reflectivity and dominant hydrometeor identification (HID) cross sections from the CHILL radar through the June 6, 2012 CO thunderstorm at 2329 UTC. (a) Reflectivity cross section along X-Z axes at $y = 22.0$ km with U, W wind vectors. (b) reflectivity cross section along Y-Z axes at $x = 24.0$ km with V, W wind vectors. Note that (c) and (d) same as (a) and (b) but for HID fields. HID fields are: not applicable (“N/A”), drizzle (“DZ”), Rain (“RA”), ice crystals (“IC”), aggregates (“AG”), snow (“SN”), vertical ice (“VI”), low-density graupel (“LG”), high-density graupel (“HG”), hail (“HA”), and big drops (“BD”). FE within 1 km of cross sections is contoured in black at 2.5, 10, 15, 20, and 25 km. Note that ground level is ~ 1.7 km for this Colorado case.

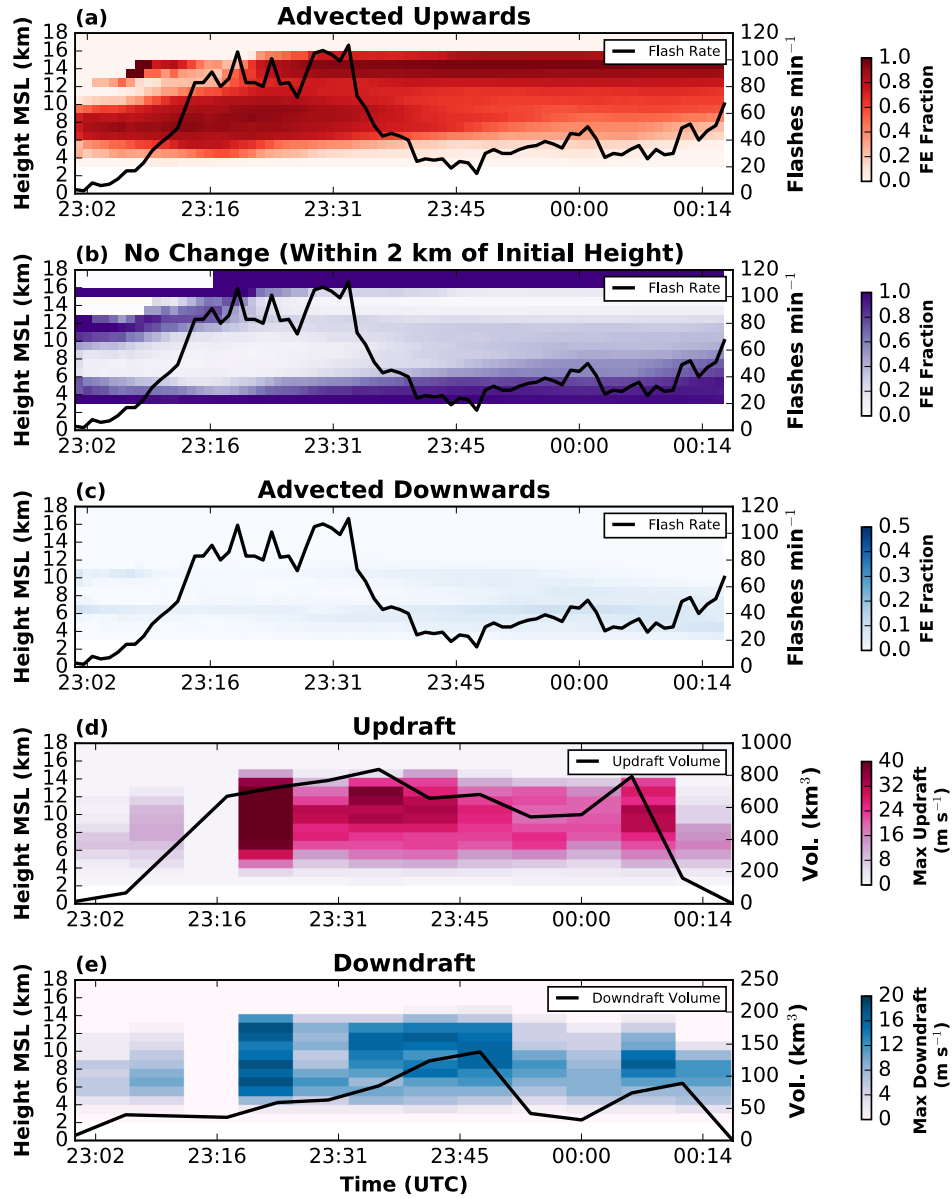
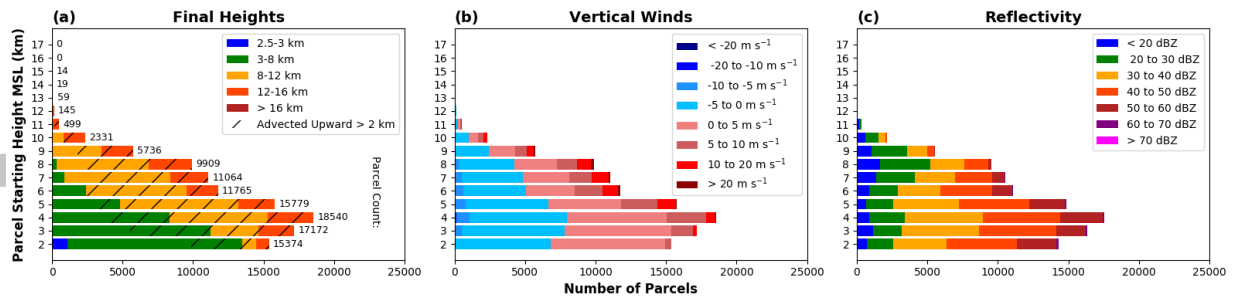


Figure 3: Time series of storm intensity parameters for the June 6, 2012 Colorado storm. (a) Time series of the fraction of total FE at each 1 km height in the storm advecting upward more than 2.0 km from initiation and flash rate (black line). (b) Time series of the fraction of total FE at each 1 km height in the storm remaining within 2.0 km of initiation and flash rate (black line). (c) Time series of the fraction of total FE at each 1 km height in the storm advecting downward more than 2.0 km and flash rate (black line). (d) Maximum updraft at each level of storm and total updraft volume exceeding 5.0 m s^{-1} (black line). (e) Maximum downdraft at each level of storm and total downdraft volume exceeding 5.0 m s^{-1} (black line). Note that ground level is $\sim 1.7 \text{ km}$ for this storm, that the range of the color bar scale for (c) is one-half that for (a) and (b), and that the right-hand axis for (e) is less than that for (d). Note that the small sample size of parcels initiating above 15 km results in fewer parcels to analyze, thus the higher fractions above 15 km in (b) are essentially meaningless.

6 June 2012 Colorado Anomalous Storm



18 May 2012 Alabama Normal Storm

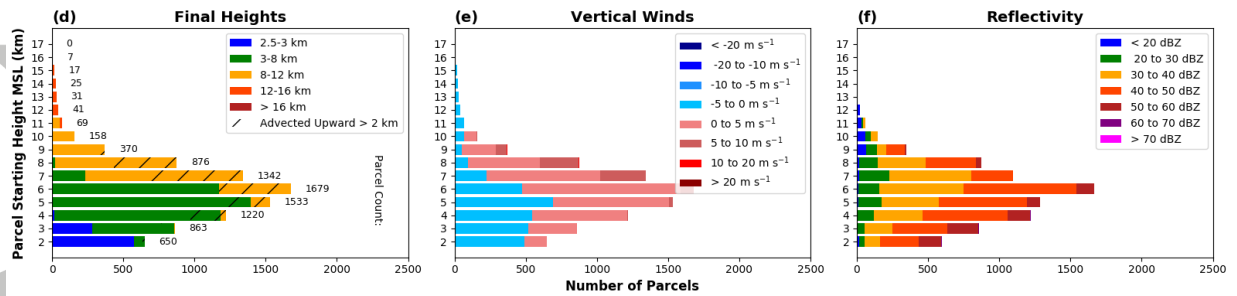


Figure 4: Bar plots of the vertical distribution of FE parcels by initiation height for the June 6, 2012 Colorado anomalous storm using the CHILL radar (a, b, c) and the May 18, 2012 Alabama normal storm using the KHTX radar (d, e, f). Parcels are binned into 1 km initial vertical height increments (note y-axis labels are lowest height in each 1 km increment). (a, d): bars are colored by final height increments parcels reach, hatching areas represent fraction of parcels that are advected upward more than 2 km from their initiation height within that level. Note that substantial downward advection of parcels more than 2 km from their initiation heights was very uncommon and thus is not depicted. Number of parcels originating within each 1 km vertical height range are listed at the end of each bar. (b, e) bars are colored by vertical wind velocity ranges in which parcels initiate at each level. (c, f): bars are colored by reflectivity volume ranges in which parcels initiate at each level. Note that ground level is ~1.7 km for the June 6 Colorado case and ~0.2 km for the May 18 Alabama case.

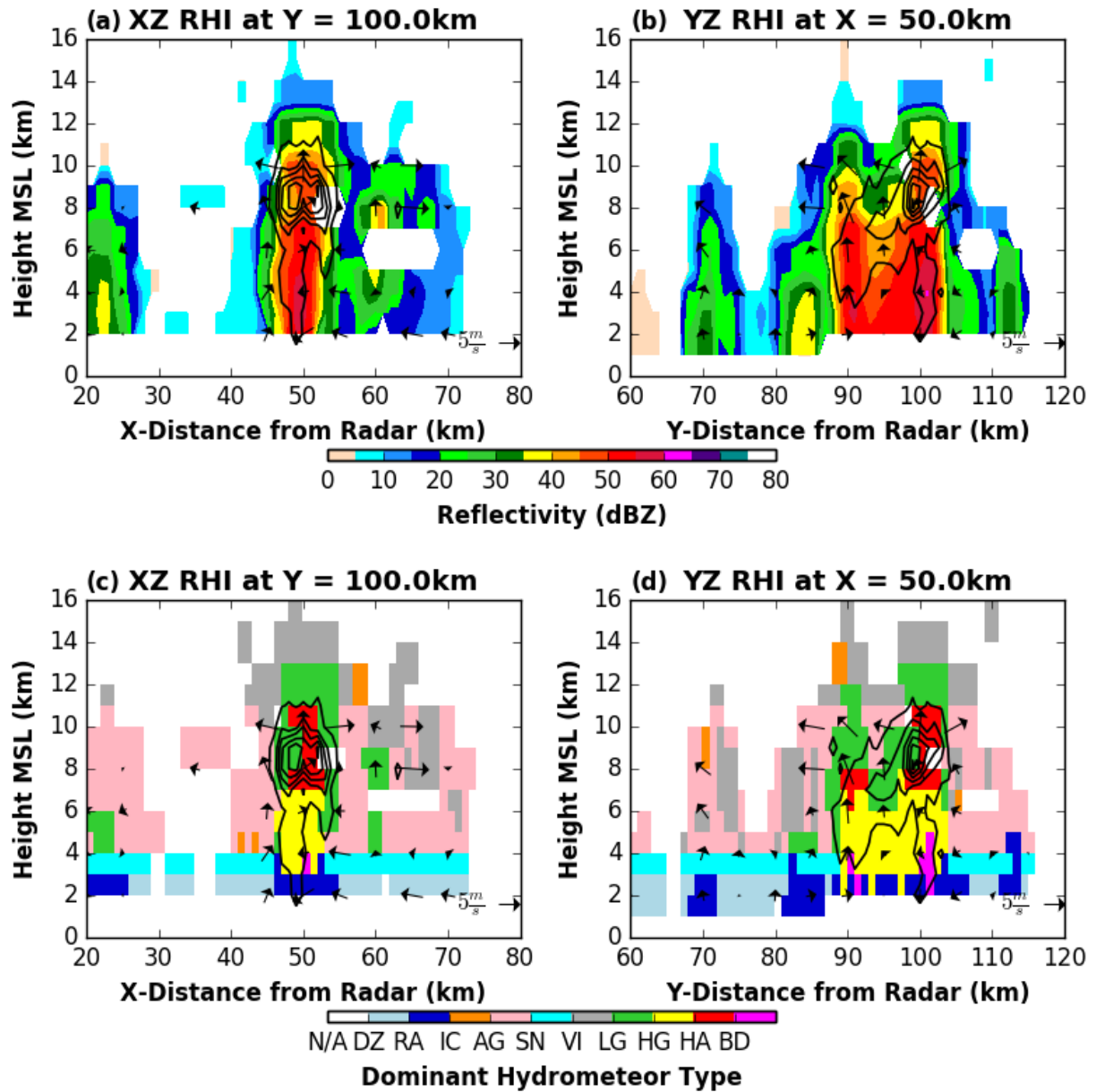


Figure 5: Reflectivity and HID cross sections from the KHTX radar through the May 18, 2012 AL thunderstorm at 2223 UTC. (a) Reflectivity cross section along X-Z axes at $y = 100.0$ km with U, W wind vectors. (b) Reflectivity cross section along Y-Z axes at $x = 50.0$ km with V, W wind vectors. Note that (c) and (d) same as (a) and (b) but for HID fields. Also, note that the wind vectors are scaled to 5 m s^{-1} versus 10 m s^{-1} in Figure 2 for the June 6, 2012 CO storm. HID fields: are not applicable (“N/A”), drizzle (“DZ”), Rain (“RA”), ice crystals (“IC”), aggregates (“AG”), snow (“SN”), vertical ice (“VI”), low-density graupel (“LG”), high-density graupel (“HG”), hail (“HA”), and big drops (“BD”). FE within 1 km of cross sections is contoured in black at 2.5, 10, 15, 20, and 25 km.

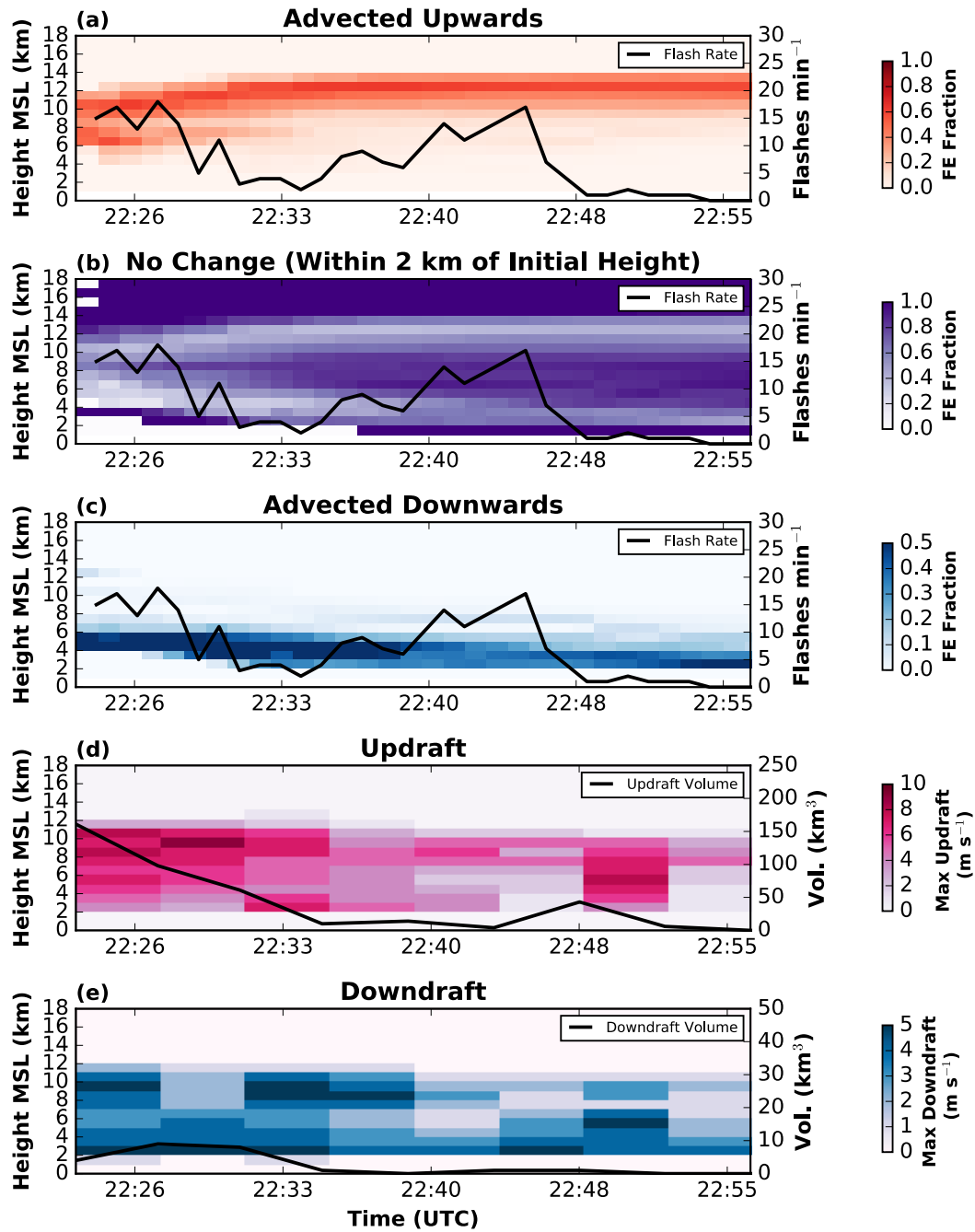


Figure 6: Same as Figure 3 except for the May 18, 2012 Alabama storm. Note ground level is around 0.2 km in this case. Also note that the color bar scale for (d) and (e) and the right hand axes for all panels are less than that shown for the June 6 Colorado storm in Figure 3d, e. Note that the small sample size of parcels initiating above 14 km results in fewer parcels to analyze, thus the higher fractions above 14 km in (b) are essentially meaningless.

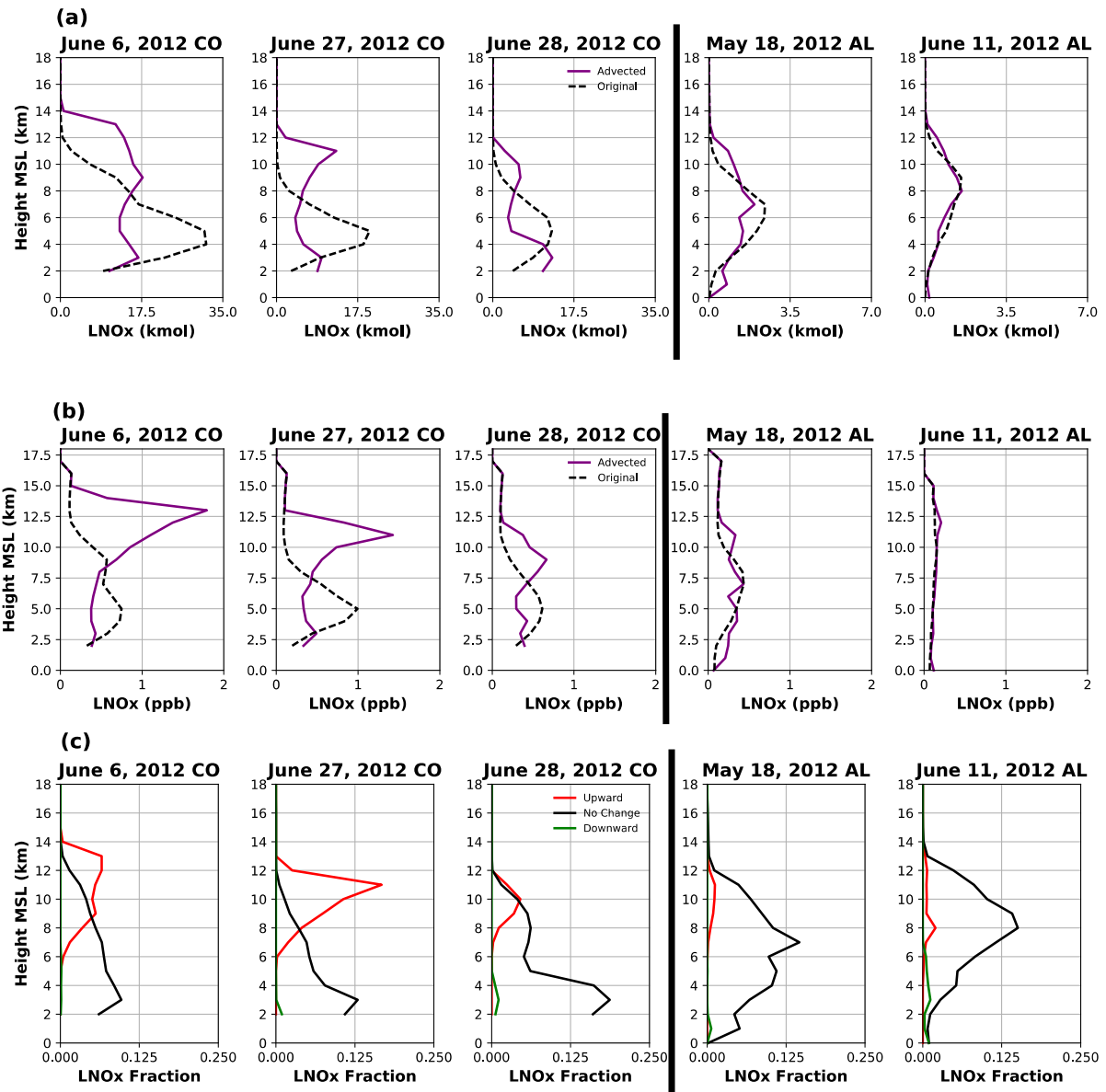


Figure 7: Vertical distribution of LNO_x for all thunderstorm cases before and after parcels have been advected in kilo moles (a) and parts per billion mixing ratios (b). (c) represent the vertical profiles of the LNO_x fraction at each level of the total LNO_x produced within each storm categorized by contributions from parcels advecting upward ≥ 2.0 km (red), from parcels remaining within 2.0 km of initiation height (black), and from parcels advecting downward ≥ 2.0 from initiation height (green). Dashed lines represent values if FE channel parcels remained stationary at initiation locations without undergoing advection and solid lines represent values after parcels have been advected over storm lifetimes. Note that the x-axes' scales for May 18 and June 11 Alabama cases are one fifth that of Colorado storm cases in plot (a). Also, note that ground level is ~ 1.7 km for the Colorado cases and ~ 0.2 km for the Alabama cases.

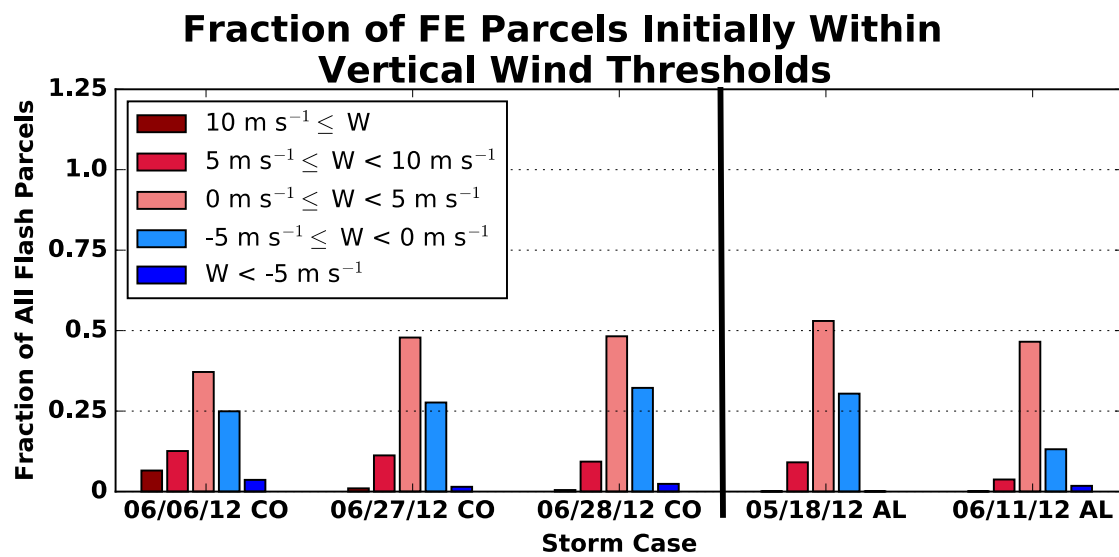


Figure 8: Fraction of total number of FE parcels initiating within various vertical velocity volumes for each of the five storms.

Table 1. Various Metrics and LNO_x Estimates for Each Storm

	6 June 2012 CO	27 June 2012 CO	28 June 2012 CO	Anomalous Mean^a	18 May 2012 AL	11 June 2012 AL	Normal Mean^a
Timespan (UTC)	2259 - 0017	2154 - 2254	2039 - 2159		2223 - 2256	2018 - 2122	
Max 20 dBZ Volume (km³)^b	3051	2125	1805	2327	2098	4000	3049
Max Updraft (m s⁻¹)	38.0	17.6	15.1	23.6	9.1	11.3	10.2
Max Downdraft (m s⁻¹)	17.9	10.1	11.3	13.1	6.4	16.6	11.5
Approx. LCL Height (MSL km)^c	3.8	3.5	4.2	3.8	1.0	0.7	0.9
Most Unstable CAPE (J kg⁻¹)^c	2712	905	10		1633	3850	
Approx. BL Height (MSL km)^c	3.6	4.8	4.8	4.4	2.5	0.8	1.7
Warm Cloud Depth (km)^d	1.94	3.64	1.55		2.97	3.88	

^aAnomalous polarity storms and means given in first four columns, normal polarity storms and means given in last three columns.

^bdBZ volume and maximum updrafts and downdrafts are calculated within each storm cell boundary extended upward along the z-axis.

^cLifting condensation levels (LCLs) and BL tops are estimated from nearest (spatially and temporally) National Weather Service soundings from the University of Wyoming and the Storm Prediction Center.

^dWarm cloud depth defined as the vertical distance between cloud base (LCL) and freezing level within each storm cloud.

Table 2. Flash Characteristics for Each Storm

	6 June 2012 CO	27 June 2012 CO	28 June 2012 CO	Anomalous Mean ^a	18 May 2012 AL	11 June 2012 AL	Normal Mean ^a
Timespan (UTC)	2259 - 0017	2154 - 2254	2039 - 2159		2223 - 2256	2018 - 2122	
Max Flash Rate^b (fl. min⁻¹)	111	65	28		18	15	
Total Flash Count^b	3737	723	680		238	267	
Flashes in Updrafts^c (w ≥ 0 m s⁻¹)	78.5%	78.6%	71.9%		76.2%	82.1%	
Flashes in Downdrafts^c (w < 0 m s⁻¹)	21.5%	21.4%	20.1%		23.8%	17.9%	
Flashes in Weak Vertical Motion^c (5 m s⁻¹ ≥ w)	64.2%	76.4%	83.7%		85.4%	92.7%	
Total FE Parcels	108406	43803	38738	63649	8881	6737	7809
Mean Initial FE Height (MSL km)	5.9	5.1	5.5	5.5	6.6	7.9	7.3
Parcels Starting Below and Ending Above 8 km	20%	35%	45%		9%	12%	
Parcels Always Above 8km	25%	10%	17%		55%	30%	
LNO_x Range (moles fl⁻¹)^d	2 – 1030	2 - 1449	5 - 1062	3 – 1180	2 – 638	3 – 269	3 – 454
Mean LNO_x per Flash^d (moles fl⁻¹)	72.4	158.0	142.8	124.4	92.5	60.7	76.6
Standard Deviation LNO_x per Flash^d (moles fl⁻¹)	111.5	178.3	140.8		103.9	66.5	
Total Storm LNO_x Produced^d (kmol)	171.8	74.6	64.8	103.7	13.3	9.3	11.3
LNO_x from Parcels Advected to UT & Upward ≥ 2 km^d	63.1%	84.2%	39.8%	62.4%	11.5%	8.4%	10.0%

Resulting LNO_x Above BL^d	84.1%	56.0%	35.4%	58.5%	96.8%	99.0%	98.4%
---	-------	-------	-------	-------	-------	-------	-------

^aAnomalous polarity storms and means given in first four columns, normal polarity storms and means given in last three columns.

^bFlashes are attributed to each storm if they occurred within the storm identified cell or up to 10.0 km outside of the cell.

^cInitial flash locations used to categorize flash location and defined as where the first flash source in the entire set of VHF sources comprising the flash occurs.

^dLNO_x production follows parameterization in Wang et al. (1998) using initial pressure of each parcel.